Reduced Indium Tin Oxide as a Transparent Superconductor

by

Emma Batson

B.S. Electrical Engineering
Massachusetts Institute of Technology (2020)

Submitted to the Department of Electrical Engineering and Computer Science
in Partial Fulfillment of the Requirements for the Degree of

Master of Science

at the

MASSACHUSETTS INSTITUTE OF TECHNOLOGY

May 2022

Signature of Author: .....

Department of Electrical Engineering and Computer Science
May 11, 2022

Certified by .....

Karl K. Berggren
Professor of Electrical Engineering and Computer Science
Thesis Supervisor

Accepted by .....

Leslie A. Kolodziejski
Professor of Electrical Engineering and Computer Science
Chair, Department Committee on Graduate Students

Reduced Indium Tin Oxide as a Transparent Superconductor

by

Emma Batson

Submitted to the Department of Electrical Engineering and Computer Science
on May 11, 2022 in Partial Fulfillment of the Requirements for the Degree of
Master of Science

ABSTRACT

Absorption of optical light in superconducting electronics is a major limitation on the quality of circuit architectures that integrate optical components with superconducting components. Such absorption causes losses in the optics and quasiparticle generation in the superconductor, decreasing the performance of both [1]. However, integration of optical and superconducting components will be crucial for the development of electro-optical transducers for quantum networking [2], scalable readout of single photon detectors [3], and neuromorphic computing [4]. Ideally, we could fabricate the superconducting electronics in these systems out of a material that is transparent to the wavelengths used by the optical components.

Few conductive materials are transparent to optical wavelengths though, let alone superconducting materials. Typical metals have a high carrier concentration and no band gap, resulting in strong absorption for light below x-ray frequencies [5]. However, certain degenerately doped semiconductors known as transparent conductive oxides have ultraviolet band gap energies, high mobilities, and low carrier concentrations, thus allowing for both good conduction and optical transparency. Under the right conditions, these materials may superconduct as well. One such material, indium tin oxide (ITO), has been shown to superconduct with a maximum transition temperature of about 4 K when doped to carrier concentrations of about $10^{21}\mathrm{cm}^{-3}$ [6]. In particular, arbitrary samples of ITO can superconduct when sufficiently doped by electrochemical reduction [7].

In this thesis, we characterize the effects of electrochemical reduction on the electronic properties, structure, and composition of ITO and evaluate its suitability for superconducting electronics. First, in Chapter 1, we outline the theory of transparent superconductivity and review existing work on such materials. Then in Chapter 2 we describe the basic theory and design of our electrochemical cell and discuss the characterization techniques we will use to evaluate our films. In Chapter 3 we present our findings on the electronic properties, structure, and composition of ITO reduced to different total reduction charge densities. In Chapter 4 we quantify the optical properties of reduced ITO and compare it to niobium, a common material for superconducting electronics. In Chapter 5 we consider different methods for fabricating electronics on reduced ITO and evaluate the resulting microwires. Finally, in Chapter 6 we discuss the implications of our findings and future directions for work on transparent superconductors.

Thesis Supervisor: Karl K. Berggren

Title: Professor of Electrical Engineering and Computer Science

Acknowledgments

The list of people whose advice, help, or encouragement made this thesis possible is too long to print, and I extend my gratitude to everyone who supported me in this time. I'd especially like to thank my advisor, Professor Karl Berggren, and my academic advisor, Dr. Donnie Keathley, for guidance in both research and writing and for establishing a group culture in which I could learn and thrive.

I would also like to thank Marco Colangelo, who not only taught me so much about experimenting with superconducting electronics but also calmly listened to much of my confusion about my data. And I'd like to thank John Simonaitis for his invaluable help in creating the experimental setup that made this work possible, and Andrew Dane for being the first in our group to start experiments along these lines and showing me the ropes.

I would also like to thank Eyosias Gebremeskel, both for assistance with sample preparation and characterization as well as his patience with my own first efforts at mentorship.

I would like to thank Mayuran Saravanapavanantham in Vladimir Bulovic's group for providing ITO on silicon, which was key to obtaining good optical data, and Professor Julia Mundy, Johanna Nordlander, Margaret Anderson, and Erika Ortega Ortiz at Harvard for providing epitaxial ITO.

I thank the National Science Foundation for supporting the Center for Quantum Networking, of which this project is a part, as well as my studies.

Finally I would like to thank my partner Angel Alvarez, to whom I have always come home these past two years, and all of the people who raised me with everything I needed to get to this point, especially my mom for all those trips to the library, my dad for an appreciation of Linux, and my sister for always backing me up when I needed it.

List of Figures

Contents

1 Introduction

Quantum electronics systems increasingly require the placement of superconducting microwave electronics on-chip with optics. Superconducting nanowire single photon detectors (SNSPDs) and images (SNSPIs) [3], for instance, may need to absorb optical photons in one part of the circuit, but still use standard microwave readout electronics for processing the resulting signals. Quantum networks will need to convert between microwave computing qubit states and optical communication qubit states, likely using electro-optical transducers [8, 9, 2] where superconducting electrodes couple to optical resonators. Similar transducers may also be needed for circuit architectures for neuromorphic computing [4].

In these systems, imperfectly confined optical fields can penetrate the superconducting electronics. Absorption of these fields in the superconductor induces losses in the optical part of the circuit and can poison the superconductor itself through quasiparticle generation [1, 10]. Optimization of the geometry can mitigate these effects but not eliminate them, since the optics and electronics still must be relatively near each other by design. Ideally, we could create these optics-adjacent superconducting electronics from a transparent superconducting material to help avoid absorption.

Although transparent conductors like indium tin oxide are well-studied and used in a variety of applications from solar cells [11] to touch screen electronics [12], creating and working with transparent superconductors presents a greater challenge. In fact, transparency and conductivity in one material already appear to present an inherent contradiction. The spectrum of wavelengths to which a given material is transparent is primarily set by two processes: absorption of light by bound electrons, set by the crystal lattice properties such as band gap, and absorption of light by free electrons, set by the dielectric constant, the electron effective mass, and the carrier concentration. In general, the more free electrons are present, the narrower the transparency window becomes. Yet increasing free electrons is also key to improving conductivity.

Still, a number of transition metal oxides strike this balance and achieve both transparency and conductivity, for instance by combining a low carrier concentration with a high mobility. Among these materials, only a few have been measured to superconduct, typically under very specific doping conditions, and the processing resulting in superconductivity has been reported

to decrease transparency [6, 7]. Even for these known candidate transparent superconductors, quantitative data on their properties is sparse.

In this thesis, we explore the material properties of candidate transparent superconductors with a focus on implications for engineering electronics. Although we will discuss several materials that have shown potential as transparent superconductors, we primarily perform our experiments on indium tin oxide (ITO), which is the most well-studied of these materials both within the context of superconductivity and across many other fields. We describe our method for producing superconducting ITO, determine the structural and compositional changes our method causes, quantify key material properties of superconducting ITO, and evaluate the suitability of our material for transparent electronics applications.

Before we consider ITO specifically, though, it will be important to first review the general theory of transparent conductors and establish its overlap with theory of superconducting semiconductors. We will then consider previous experiments with superconductivity in transparent conductors and how they fit into these theories.

1.1 Transparency in Conductors

In order to study and engineer transparent conducting materials, we must understand the relationship between conductivity and transparency so we can navigate the trade-offs between them. For this and future discussions, we will define transparency as a low extinction coefficient for wavelengths around optical frequencies. In this section, we will show how key electronic properties, namely free carrier concentration, effective mass, and dielectric permittivity, determine a material's transparency window. Next we will consider several superconducting materials derived from optically transparent conductors, which still remain more transparent than a typical metal after treatment.

1.1.1 Optical Processes

In general, optical processes in a material fall into one of two categories. First, intraband processes involve electronic conduction by free carriers. These will be the dominant processes in highly conductive materials, like metals or degenerate semiconductors, and they can be understood by

examining the limiting cases of the Drude model. Intraband processes determine absorption for low-energy photons. Second, interband processes involve photon absorption that takes an electron from an occupied state in the valence band to an unoccupied state in the conduction band. For semiconductors, these processes mostly occur for photons with energies greater than the band gap, so high-energy transparency simply necessitates a large band gap.

The band gap is set by lattice properties and is not easily tunable, but, as we will see shortly, the intraband behaviors can be changed by carrier doping. Thus here we will focus on intraband optical processes. Following Millie Dresselhaus's derivation [13], we will begin by constructing a classical model of conductivity in solids, known as the Drude model. We can start with the classical equation for velocity of a free carrier:

$$m\frac{d\vec{v}}{dt} + \frac{m\vec{v}}{\tau} = e\vec{E}_0 e^{-i\omega t} \tag{1}$$

Here, m is the effective mass of the electron in the material; τ is the scattering time for electrons; and e is the charge of the electron. The solution to this equation in a sinusoidal field yields the following:

$$(-im\omega + \frac{m}{\tau})\vec{v}_0 = e\vec{E}_0 \tag{2}$$

Next we use the definition of current density to relate this equation to conductivity:

$$j = ne\vec{v_0} = \sigma\vec{E}_0 \tag{3}$$

In this equation, we introduce n, the concentration of free carriers (here, electrons) in the material. With some algebraic manipulation, we find equation 4, the which relates conductivity to frequency and fundamental material parameters:

$$\sigma = \frac{ne^2\tau}{m(1 - i\omega\tau)} \tag{4}$$

Additionally, we define the complex permittivity of a material, which follows from allowing an absorptive, imaginary term in the complex wave equation:

$$\epsilon_{complex} = \epsilon + i\frac{4\pi\sigma}{\omega} = \epsilon_1 + i\epsilon_2 \tag{5}$$

Here we may also define the complex refractive index, in equation 7, which is another way of expressing the complex permittivity that may be more convenient for some of our later calculations, particularly for net absorption. The quantity n is the usual real part of the refractive index, and k is the extinction coefficient.

$$\epsilon_1 = n^2 - k^2 \tag{6}$$

$$\epsilon_2 = 2nk \tag{7}$$

By plugging equation 4 into equation 5, we can examine the frequency dependence of the permittivity. The full equation for complex permittivity in these terms is given in equation 8, where ϵ_∞ is a constant representing the contribution to permittivity from processes besides free carrier intraband absorption.

$$\epsilon = \epsilon_1 + i\epsilon_2 = \epsilon_\infty + i\frac{4\pi}{\omega}\frac{ne^2\tau}{m(1 - i\omega\tau)} \tag{8}$$

At low frequencies, we take the following approximation:

$$\epsilon \approx \epsilon_\infty + i\frac{4\pi ne^2\tau}{m\omega} \tag{9}$$

Now as ω approaches 0, the imaginary component of the permittivity dominates. Key features of the low-frequency regime that can be derived from these equations are that $n \approx k$ and that reflectivity is nearly unity. Additionally, the real part of the permittivity will typically be negative for a good conductor in this regime.

At high frequencies, the equation for permittivity approaches the following:

$$\epsilon \approx \epsilon_\infty - \frac{4\pi ne^2}{m\omega^2} \tag{10}$$

Notably, the intraband term that provides the characteristic behavior of a conductor becomes

very small at high frequencies. As a result, the effects of interband processes will dominate, and the metal behaves more like a dielectric in this regime.

Clearly, good conductors will be reflective rather than transparent in the low frequency regime, but may be transparent somewhere in its dielectric regime. A crucial question for us, then, is the determination of where this transition from conductor to dielectric occurs.

1.1.2 Plasma Frequency

The characteristic frequency at which a material's behavior changes from metallic to dielectric is called the plasma frequency. More precisely, since metallic behavior involves a negative permittivity and dielectric behavior a positive permittivity, the plasma frequency is the frequency at which the real part of the permittivity goes to 0. With some algebraic manipulation of equation 8, we can separate out the real and imaginary parts into equations 11 and 12.

$$\epsilon_1(\omega) = \epsilon_\infty - \frac{4ne^2\tau^2}{m(1+\omega^2\tau^2)} \tag{11}$$

$$\epsilon_2(\omega) = \frac{4\pi}{\omega}\frac{ne^2\tau^2}{m(1+\omega^2\tau^2} \tag{12}$$

We can set equation 11 to zero to solve for the screened plasma frequency, $\hat{\omega}_p^2$. It is considered "screened" by the core dielectric constant of the medium which has been set by other processes, while the "unscreened" plasma frequency sometimes quoted in the literature is computed by setting the core dielectric constant equal to one.

$$\hat{\omega}_p^2 = \frac{4\pi ne^2}{m\epsilon_\infty} - \frac{1}{\tau^2} \tag{13}$$

The plasma frequency helps us think about the reflectivity of a good conductor at different frequencies. For very low frequencies, a good conductor has metallic behavior, and should be a nearly perfect reflector. At frequencies well above the plasma frequency, we expect dielectric behavior. There may be some reflection, but not much. However, at exactly the plasma frequency, the real part of the permittivity is zero, and there is essentially no reflection.

Therefore, below a material's plasma frequency, we expect high reflectivity and therefore

also high absorption (since $n \approx k$ in the low-frequency regime). It is only above the plasma frequency that low absorption and transparency become possible. Hence the "redder" end of the transparency window is set by the plasma frequency (the "bluer" end is typically set by interband processes, particularly the band gap, since at high frequencies the conductor exhibits dielectric behavior).

Note, in particular, that the plasma frequency increases with free carrier concentration, and decreases with increased effective mass and core dielectric constant. Most conductors have a high carrier concentration, and low-to-intermediate effective mass and dielectric constant, typically resulting in plasma frequencies in the petahertz range [5]. However, by searching for conductors with lower carrier concentrations or higher effective mass and dielectric constant, we can perhaps find transparent conductors and even transparent superconductors.

In practice, there are many other processes that will affect transparency, particularly in ITO, including crystallinity [14] and even geometric effects like plasmonics [15]. However, understanding the bulk plasma frequency provides a simple and helpful tool for comparing potential transparent conductors and making a priori guesses about which materials might be suitable for transparent superconductivity.

1.1.3 Quantifying Transparency

Although the previous calculations give us some idea of what material parameters could lead to visible transparency, we will need to actually quantify the transparency of real materials we develop in order to determine whether they could be useful for the desired applications. For this we must go beyond the refractive index and derive from them the transmittance, reflectance, and absorptance of our films using the Fresnel equations [16, 13]. We will assume electromagnetic radiation with magnitude E_{0i} incident on an interface as shown in Figure 1. The proportion which is reflected, E_{0r}, to the proportion transmitted, E_{0t}, will be dependent on the angle of incidence θ_i and on the complex refractive indices of the materials on either side of the interface, $n_1 - ik_1$ and $n_2 - ik_2$.

Electromagnetic radiation must satisfy equations for continuity and differentiability at an interface. These differ slightly depending on the polarization of the light. First let us consider light perpendicularly polarized relative to the plane of incidence, also known as s-polarized light,

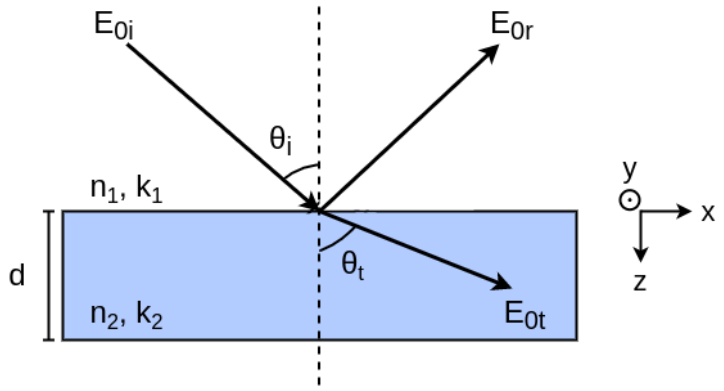

Figure 1: In this figure we see an incident electromagnetic wave with magnitude E_{0i} incident on an interface at some angle θ_i. There will be some resulting reflection with magnitude E_{0r} and some resulting transmission with magnitude E_{0t}, which can be computed from the Fresnel equations using the complex refractive indices of the materials on either side of the interface, $n_1 - ik_1$ and $n_2 - ik_2$.

given in equations 14 and 15.

$$E_{0i} + E_{0r} = E_{0t} \tag{14}$$

$$-B_{0i}\cos\theta_i + B_{0r}\cos\theta_r = B_{0t}\cos\theta_t \tag{15}$$

We can simplify these equations because we know that $\theta_i = \theta_r$ and that $B = (n - ik)/c \times E$. We can combine this information into equation 16.

$$(n_1 - ik_1)(E_{0r} - E_{0i})\cos\theta_i = (n_2 - ik_2)(E_{0r} + E_{0i})\cos\theta_t \tag{16}$$

From here we can define the perpendicular Fresnel reflection coefficient, r_s.

$$r_s = \frac{E_{0r}}{E_{0i}} = \frac{(n_1 - ik_1)\cos\theta_i - (n_2 - ik_2)\cos\theta_t}{(n_1 - ik_1)\cos\theta_i + (n_2 - ik_2)\cos\theta_t} \tag{17}$$

For parallel polarized, or p-polarized, light, the boundary counditions are similar to equations 14 and 15, but the roles of the electric and magnetic fields are flipped. As a result, the Fresnel reflection coefficent r_p is given as in equation 18.

$$r_p = \frac{(n_1 - ik_1)\cos\theta_t - (n_2 - ik_2)\cos\theta_i}{(n_1 - ik_1)\cos\theta_t + (n_2 - ik_2)\cos\theta_i} \tag{18}$$

These definitions will be useful later, but we quickly see that, in general, they are not sufficient for computing reflections off an interface involving a complex refractive index. The usual Snell's law, $\tilde{n}_i \sin\theta_i = \tilde{n}_t \sin\theta_t$, yields a complex θ_t if $\tilde{n}_t$ is complex. Clearly, this is not what we usually mean by transmission angle. We will need to derive some additional constraints in order to solve for this angle, following Bousquet's derivation [17].

We will start at the beginning, with the general solution to the electromagnetic wave equation in equation 19, where α_i, β_i, and γ_i describe the relative velocity of light in the material in the respective layer. In the coordinate system we have defined, $\beta_i = 0$ because it is perfectly parallel to the interface, while $\alpha_i = (n_i - ik_i)\sin\theta_i/c$ and $\gamma_i = (n_i - ik_i)\cos\theta_i/c$.

$$\vec{E_i} = \vec{E}_{0i} \exp[i\omega(t - (\alpha_i x + \beta_i y + \gamma_i z)] \tag{19}$$

The Snell-Descartes law furthermore ensures that $\alpha_1 = \alpha_2$. We rewrite our reflectances in terms of these constants below.

$$r_s = \frac{\gamma_2 - \gamma_1}{\gamma_2 + \gamma_1} \tag{20}$$

$$r_p = \frac{\epsilon_{x2}\gamma_1 - \epsilon_{x1}\gamma_2}{\epsilon_{x2}\gamma_1 + \epsilon_{x1}\gamma_2} \tag{21}$$

Now for the case of perpendicular polarization, by definition only the y component of the electric field and the x component of the magnetic field are nonzero. Maxwell's equations produce the following relationship between the electric field and the displacement field:

$$\frac{1}{c^2}\frac{\partial^2 \vec{D}}{\partial t^2} = \Delta\vec{E} - \nabla(\nabla \cdot \vec{E}) \tag{22}$$

Because we are solving for electromagnetic waves, we can plug in the sinusoidal forms of $\vec{D}$ and $\vec{E}$ to obtain additional relationships:

$$\frac{1}{c^2}\frac{\partial^2 \vec{D}}{\partial t^2} = -\omega^2 \vec{D} \tag{23}$$

$$\Delta \vec{E} = -\omega^2(\alpha^2 + \beta^2 + \gamma^2)\vec{E} \tag{24}$$

$$\nabla \cdot \vec{E} = -i\omega(\alpha E_x + \beta E_y + \gamma E_z) \tag{25}$$

Then, setting the appropriate values to zero and substituting the usual $D_i = \epsilon_i E_i$ and the above equations into equation 22, we can derive a relationship between γ and α.

$$\frac{1}{c^2}\epsilon_y = \alpha^2 + \gamma^2 \tag{26}$$

Furthermore, because $\alpha_1 = \alpha_2$, we can finally write γ_2 in terms of only optical constants and the incident angle.

$$\gamma_2^2 = \frac{\epsilon_{y2}}{c^2} - \alpha_1^2 \tag{27}$$

The derivation for the parallel component is similar, but the roles of the electric and magnetic fields are again flipped.

$$\gamma_2^2 = \frac{\epsilon_{x2}}{c^2} - \alpha_1^2\frac{\epsilon_{x2}}{\epsilon_{z2}} \tag{28}$$

If the material is isotropic, this simplifies to equation 27. Now we have sufficient information to compute the transmission angle and the Fresnel reflection coefficient for incidence on materials with a complex refractive index, as long as we know the optical constants and the angle of incidence. The total reflection is given by the magnitude squared of the reflection coefficient.

Any radiation not reflected at the interface is transmitted into the second material. However, if the second material is absorptive, then the total transmittance is reduced by the amount of light absorbed. The total transmittance can be computed fairly simply from the extinction coefficient, thickness of the material, and angle of transmission. For simplicity we will assume an isotropic material for this derivation. First we write out the solution to the wave equation for a material with a complex refractive index and rearrange it.

$$\vec{E} = \vec{E}_0 \cos\omega(t - \frac{n - ik}{c}\vec{r}) \tag{29}$$

$$= \vec{E}_0 \exp\left[\frac{-\omega k}{c}\vec{r}\right] \cos\omega(t - \frac{n}{c}\vec{r}) \tag{30}$$

Then we see that the intensity of the material beyond the interface, $I(\vec{r}) = |E(\vec{r})|^2$, can be expressed as in equation 31, where $I_{0t} = I_{0i}(1 - R)$ is the intensity of light that is not reflected.

$$I(\vec{r}) = I_{0t} \exp[-\alpha\vec{r}] \tag{31}$$

In this expression, the extinction coefficient α is defined as $\alpha = 2(\omega k)/c$. Then transmittance may be defined simply as the proportion of intensity at a depth t to the initial intensity, where $t = \cos\theta_t/d$ is the total distance the light must travel through the material. For the case of transmittance in a material after passing through an interface, we specifically want to compare the intensity of absorbed light to that of the incident light.

$$T = \frac{I(t)}{I_{0i}} = \frac{I_{0i}(1 - R)\exp[-\alpha t]}{I_{0i}} = (1 - R)\exp[-\alpha y] \tag{32}$$

Any remainder that is neither reflected nor absorbed must be transmitted. So absorptance of the film can be computed from the reflectance and the transmittance.

$$A = 1 - R - T \tag{33}$$

We note here that the worst problems of having optics on-chip with superconducting electronics, that is, quasiparticle formation and reduction of optical quality factor, are most directly caused by absorption. So to be precise, when we speak of transparent superconductors for engineering applications, we actually would most prioritize a material with the lowest absorptance rather than the highest transmittance, which are often but not always synonymous. A film with a very high reflectance or which is very thin could yield the desired behavior just as well as a material with a low extinction coefficient.

However, reflectance and film thickness are not intrinsic properties of a material but depend

on the surrounding materials and required design thickness, respectively. As a result, films with low extinction coefficients are the most generally transparent in different situations.

1.2 Superconducting Semiconductors

Since candidate transparent superconductors will likely have low carrier concentrations and an ultraviolet band gap, they will probably be highly doped semiconductors or other similar materials. Interest in superconducting semiconductors has waxed and waned over the decades[18], and to our knowledge no unifying general theory exists to describe their behavior. However, existing research on superconducting semiconductors reveals enough common properties that a discussion can help guide our expectations for what a transparent, superconducting semiconductor might be like.

First we should note that pure semiconductors cannot typically superconduct, since the semiconductor band gap is much larger than the superconducting gap energy for most materials [19], especially if we are primarily seeking materials with an ultraviolet band gap. However, in degenerately doped semiconductors, the conduction band remains filled even as the temperature approaches 0 K, allowing for the possibility of superconductivity. We can use the Mott criterion to approximate necessary doping levels to achieve degeneracy for a given material [20].

Degenerately doped semiconductors differ significantly from typical metallic superconductors in two key ways. First, a superconductors like niobium or aluminum typically have carirer concentrations on the order of $10^{22}\mathrm{cm}^{-3}$

Still, while a typical metallic superconductor like niobium might have carrier concentrations on the order of 10^{22} cm^{-3} [21] or higher, degenerately doped superconducting semiconductors often have carrier concentrations in the range of $10^{18} - 10^{22}$ cm^{-3} [22] – reaching orders of magnitude lower, and also far more tunable. At these relatively low carrier concentrations, only a small part of the conduction band is filled, and so the band structure itself plays a more significant role in electron-electron interactions. Standard BCS theory alone may not be sufficient to fully explain the superconducting properties of semiconductors due to neglect of contributions from different kinds of phonon interactions.

Superconducting semiconductors usually exhibit dirty type II superconducting behaviors with transition temperatures lower than 10 K [22]. Since standard BCS theory does not account for

band structures, new approaches are required to successfully predict these transition temperatures.

Additionally, the transition temperature of superconducting semiconductors is typically dependent on the carrier concentration. For some semiconductors such as tellurides, the transition temperature monotonically increases with carrier concentration for the measured ranges. These materials are best understood through a modified version of the Morel-Anderson theory of superconductivity in the very dirty limit [23] combined with McMillan's framework for strongly-coupled superconductors [24], as outlined by Hulm et al [25].

The approximations in this theory work for dirty superconductors where the Fermi energy is much greater than typical phonon energies, and where static screening of the Coulomb potential can be assumed for frequencies below the plasma frequency. For semiconductors with these properties, normal electron-phonon interactions and Coulombic interactions decrease as carrier concentration increases due to electronic screening, while umklapp electron-phonon interactions increase with carrier concentration due to enlargement of the Fermi surface. The net effect is a prediction of the monotonic increase of transition temperature with carrier concentration, in alignment with experimental data.

For other semiconductors, such as strontium titanate [19], molybdenum sulfide [26, 27], titanium selenide [26], and potassium tantalate [28], the transition temperature has a dome-shaped dependence on carrier concentration. This behavior cannot be explained by the Morel-Anderson-McMillan framework. One alternative model proposed by Cohen focuses on multivalley semiconductors [29]. These materials can have strong interactions from intervalley phonons, which involve large momentum transfers and therefore are not screened much, and may also provide a large number of scattering states if there are many valleys. Then the intervalley phonon effects tend to dominate over intravalley phonon interactions.

Calculations using this model to predict the transition temperature of strontium titanate as a function of carrier concentration exhibit the same dome-shaped dependence as experimental data [30]. They attribute this shape to the differences between the screening dynamics of intervalley interactions versus intravalley interactions. At low carrier concentrations, more carriers primarily serve to increase the density of states, therefore increasing interaction strength and transition temperature. However, intervalley interactions are more effectively screened at high

carrier concentrations, thus decreasing interaction strength. Above a certain point, the increased screening begins to mitigate and eventually reverse the effects from increased density of state, resulting in the dome shape [31]. Similar calculations have been used to explain the dome-shaped transition temperature dependence in monolayer molybdenum sulfide [27].

Unfortunately, these theories of superconducting semiconductors require extensive knowledge of normal state material parameters in order to predict properties like transition temperature dependence on carrier concentration, and there do not seem to be simple metrics to help guess a priori, for instance, whether the transition temperature follows a monotonic or dome-shaped dependence on carrier concentration. Still, by examining these theories, we have developed some idea of what behaviors we could expect from a superconducting semiconductor like ITO.

1.3 Previous Research on Transparent Superconductors

Previous attempts have been made to turn known transparent conductors into transparent superconductors, including studies on indium tin oxide, indium oxide, indium zinc oxide, lithium titanium oxide, and lithium-deficient lithium niobate. We will consider each of these materials in turn, and discuss what they may have in common and how they may differ. We will discuss ITO first and in the most detail, since it has the greatest variety of papers focused on its suitability for transparent superconductivity or electronics.

1.3.1 As-Grown ITO

Perhaps the first report of superconductivity in ITO occurred in samples generated by Ohyama et al. [32]. Their samples were reactively magnetron sputtered from indium-tin alloy of 90 wt % indium, 10 wt % tin in an oxygen-argon atmosphere onto room temperature glass and post-annealed for thirty minutes at 400°C [33]. Uniformly distributed grains about 100 nm in diameter were observed via electron microscope. They produced samples at different thicknesses and carrier concentrations, though all carrier concentrations were on the order of $10^{20}\mathrm{cm}^{-3}$. They do not provide any data or commentary on the transmittance of these films.

Their thickest sample, at 2$\mu\mathrm{m}$, had a large resistivity drop starting just above 2 K, though it did not reach zero resistance by the lowest measured temperature of 1.5 K. Magnetoresistance

measurements provide further evidence of superconducting behavior. Comparing the resistance curve data with theoretical predictions, they estimate the transition temperature of the film to be at about 1.2 K. Although the film was quite thick, its behavior was consistent with superconductivity in a two-dimensional system. In other samples, they discuss competition between weak electron localization and superconductivity.

Chiu et al. [34] produced single-crystal ITO nanowires by thermal evaporation onto silicon with a substrate temperature of either 850°C or 900°C, set by distance from the heated source powders. The crystals grew along the [100] direction, and chemical composition and diameter of the resulting wires were found to depend on the substrate temperature. They measured the four-probe resistance of four of these wires down to 1.5 K. One wire, deposited on a closer, higher-temperature substrate, exhibited a large resistivity decrease with an onset near 5 K. This wire had the largest diameter (220 nm) and lowest room-temperature resitivity (137 $\mu\Omega\mathrm{cm}$) of the set of wires. However, the decrease is quite broad and does not reach zero resistance over the measured temperature range. The authors hypothesize that the wire's potential superconductivity is hindered by the large number of point defects observed in their material, and propose that especially high-quality, low-resistivity single-crystalline ITO may be better suited for superconducting applications. This paper is especially promising, as it shows that ITO can be suitable for superconducting electronics.

These results give a strong indication that ITO can be inherently superconducting in nature, but suggest that further engineering is required to reliably produce superconducting ITO with practical electronics applications. On the other hand, these results also show that extremely different form factors of ITO, both sputtered and single-crystalline, exhibit similar superconducting behaviors, providing a huge space within which to engineer the properties of ITO.

1.3.2 Oxygen-Deficient Annealed ITO

Mori [6] later produced superconducting ITO films via low-temperature annealing after film growth. Their films were prepared with electron-beam evaporation from indium oxide and tin oxide sources onto polyester or glass. The resulting films were 20 nm thick. Then they annealed these samples in air between 130 - 170°C for 30 - 120 minutes. Only films annealed for short times at intermediate temperatures or long times at low temperatures were found to superconduct. Too

much or too little annealing did not result in superconductivity. Increased annealing time and temperature both resulted in increased transmittance.

The superconducting films were found to be two-dimensional, dirty type-II superconductors with carrier concentrations on the order of $10^{21}\mathrm{cm}^{-3}$. The less-annealed and most-annealed films had the lowest carrier concentrations. The transition temperatures follow a dome-shaped dependence on transmittance, with a maximum $T_c \approx 4$K at 60% transmittance for 550 nm. XPS data implies the presence of oxygen deficiencies introduced by the annealing process. Therefore, it seems that the annealing process effectively dopes the ITO with oxygen vacancies, increasing the carrier concentration and enabling superconductivity.

Mori's method outlines a highly convenient procedure for fine-tuning the properties of sputtered ITO to achieve superconductivity. However, it is not clear whether this procedure can work, for instance, with ITO that has previously been annealed at a high temperature or deposited on a high-temperature substrate, so it may only be a viable strategy for labs with complete control over the ITO growth process.

1.3.3 Electrochemically Reduced ITO

More recently, Aliev et al. [7, 35] found that commercially obtained ITO on glass substrates can be doped via electrochemical reduction in various solutions of cation salts in water or propylene carbonate. They were able to control the final carrier concentrations of their films simply by adjusting the length of the reduction time. As in Mori's work, the transition temperature had a dome-shaped dependence on carrier concentration, with a maximum value near 5 K corresponding to a carrier concentration of about $1.05 \times 10^{21}\mathrm{cm}^{-3}$. According to their simulations, this carrier concentration also corresponded to a maximum density of states at the Fermi level. They describe their material as a dirty, type-II superconductor in the strong coupling regime, which aligns well with expectations from superconducting semiconductor theory. Intriguingly, the color changes and onset of superconductivity can be reversed by simply reversing the current in the electrochemical cell.

Aliev et al. attribute the increase in carrier concentration to intercalation of sodium or other small cations into the ITO lattice into oxygen vacancy 16c sites, a hypothesis which is consistent with comparisons of simulated and experimental XRD data. They additionally report observa-

tion of the paramagnetic Meissner effect in superconducting ITO films, an unusual attraction of magnetic field rather than expulsion which might arise due to flux trapping by inhomogeneities in superconducting thin films [36].

Their method of generating superconducting ITO thin films is promising for its generality, easy tunability, and accomplishment of the highest reported transition temperature yet. Moreover, although research into electrochemically doped superconducting ITO is new and limited, use of ITO as an electrochemical cathode has been broadly studied in general.

1.3.4 Indium Oxide

Indium oxide, the parent material for ITO, can itself superconduct without extrinsic dopants as long as its carrier concentration is high enough. It has proven to be of great interest for the study of amorphous superconductors and disorder effects on superconductivity. Most work on indium oxide focuses on inducing a superconductor-to-insulator transition in the material [37, 38, 39]. A superconducting transition has been observed in indium oxide wires as well, though the wires exhibited a broad transition that saturated at a finite resistance, which was attributed to excitation of phase slips [40]. The saturation value was dependent on the cross-sectional area of the wire.

1.3.5 Indium Zinc Oxide (IZO)

Indium zinc oxide (IZO) is a transparent conducting oxide similar to ITO, but doped with zinc oxide instead of tin oxide [41]. Much like with ITO, indium zin oxide carrier concentration is typically in the $10^{19} - 10^{21}\mathrm{cm}^{-3}$ range, and is primarily doped by oxygen vacancies and zinc ions (Zn^{2+}) [41, 42, 43]. Makise et al.[43] sputtered films from indium-oxide-zinc-oxide alloy targets with different zinc oxide concentrations onto a room temperature substrate and then annealed the films in air at 200 or 300°C for anywhere from 30 minutes to 48 hours. The resulting films were polycrystalline.

Transition temperatures as high as about 3.5 K were observed, with longer annealing times corresponding to higher transition temperatures. For the measured films, transition temperature monotonically decreased with carrier concentration, though they remark that they expected a dome-shaped dependence and they likely did not study films with a sufficiently low carrier concentration to observe the other half of the dome. All in all, this work on IZO has a lot in

common with Mori's work on air-annealed ITO, even exhibiting similar transition temperatures and carrier concentrations. Further comparisons of similar transparent conductive oxides may be warranted.

1.3.6 Lithium Titanium Oxide ($LiTi_2O_4$)

Lithium titanium oxide (LTO or $LiTi_2O_4$) is a transparent conductor with a very high carrier density (on the order of $10^{22}\mathrm{cm}^{-3}$) and as such can potentially support a higher transition temperature than ITO [44]. Specifically, it is a transparent spinel compound [45]. The first samples measured to superconduct were not transparent thin films but sintered pellets that were reportedly dark blue in color, with transition temperatures from 7 - 13.7 K, quite high for an oxide.[46] In a deeper study, Johnston et al.[47] showed that non-stoichiometric samples with titanium deficiencies had lower transition temperatures. They also found that, unlike ITO and IZO, LTO cannot appropriately be described as a doped semiconductor, because lithium does not act as a donor to the titanium oxide system. More precisely, the onset of metallic behavior in the system does not come from impurity band conduction. Notably, stoichiometric LTO has a higher transition temperature than LTO with enhanced lithium quantities[47]. In general, LTO has a number of properties that make it unusual, and perhaps fundamentally unlike the degenerately-doped superconducting semiconductors discussed earlier[48].

More recent work on LTO thin films by Ohsawa et al.[49] shows that its unusual nature could make it an especially promising transparent superconductor. Its bandgap of 3.3 eV, while smaller than that of ITO, is still large enough to permit transparency. Looking back at equation 13, we see that the plasma frequency may be lowered by either a low carrier concentration, as with ITO, or by a high effective mass or core permittivity. LTO has both a high effective mass and a high core permittivity, so it can support this high carrier density while keeping the plasma frequency out of the visible spectrum. However, thin films of LTO still have a distinctive blue tinge, as they do absorb more on the red side of the spectrum than materials like ITO [44]. Their 120-nm-thick epitaxially grown samples exhibited a transition temperature of 11.5 K and upwards of 60% transmittance for the visible spectrum, making it comparable in transparency to Mori's annealed ITO.

1.3.7 Lithium-Deficient Lithium Niobate ($Li_{1-x}NbO_2$)

Lithium-deficient lithium niobium oxides function as p-type doped transparent conductors. They allow about 70% transmittance up to at least 1100 nm and exhibit superconductivity below 4.2K.[50] The fabrication process requires several steps to ensure only lithium-deficient phases of the oxide are present (through a process called "deintercalation"), as the hole-doped oxide exhibits better optical transparency as well as superconductivity. Like LTO, it is typically grown on a spinel substrate.

The material also has a very high effective carrier mass, which as with LTO keeps the plasma frequency above the visible range even with carrier concentrations around $10^{22}\mathrm{cm}^{-3}$. Interband optical absorption is also suppressed by isolation of the niobium $4d_{z2}$ band. This material seems difficult to fabricate but otherwise has relatively favorable properties.

1.4 Material Properties of ITO

For our studies, we focus on ITO, since it is the most readily available, widely studied, and easily tunable of the candidate transparent superconductors. Moreover, there are many potential superconducting materials with similar physics as ITO, such as other derivatives of indium oxide or possibly zinc oxide, so our results with ITO may be useful guides for those as well.

ITO is a fairly complex material whose electrical and optical properties are strongly dependent on the film thickness, preparation technique, and growth conditions.[51] ITO has a cubic bixbyite crystal structure with 48 crystallographically equivalent sites for oxygen, leaving 16 vacancies per unit cell.[7] This makes for a flexible and sensitive crystalline structure, the composition of which might be altered post-deposition by factors such as oxygen deficiency or ion intercalation [52, 7]. However, the initial deposited layers of ITO tend to have heavily disordered microstructures, resulting in inhomogeneous distribution of free carriers and a strong vertical grading of the film properties [52].

ITO has been deposited on crystalline silicon, polyester, and various glass substrates, and each substrate can result in slightly different properties, particularly in the superconducting form [6]. ITO can also be epitaxially grown into very thin films on yttrium-stabilized zirconium, which matches the crystal structure [53, 54].

This leaves us with a huge parameter space for engineering the material properties of ITO. Depending on how it is deposited, annealed, or post-treated, we can achieve a wide range of electrical and optical properties. The simplest method of tuning carrier concentration, and the one we will focus on here, is electrochemical reduction.

2 Methods

In this section we describe the methods used to generate and characterize reduced ITO samples. This includes a brief description of different electrochemical techniques that were considered as well as descriptions of key methods in material analysis: scanning transmission electron microscopy with energy-dispersive x-ray spectroscopy (STEM-EDS), x-ray photoelectron spectroscopy (XPS), and ellipsometry.

2.1 Electrochemical Reduction

Electrochemical reduction is a convenient way to change carrier concentration of a material. Reduction can be carried out with safe, easy-to-handle materials such as saltwater, and at low currents and voltages with any sufficiently stable source and measurement set-up. The experiment can be carried out in almost any lab space. However, care must be taken to ensure the electrochemical cell is stable and repeatable enough to perform many reproducible experiments.

The basic idea of electrochemical cells is simple: apply a current between two electrodes submersed in an ionic solution, thus inducing a current carried by the ions inside the cell. When the ions reach the surface of the electrodes, reactions can occur. However, the microscopic reality of an electrochemcial cell is more complicated, and in some ways the dynamics are more analogous to those of a doped semiconductor junction than to lumped electronics.

We will discuss the most significant aspects of electrochemical cell dynamics and how they apply to design of our reduction cell.

2.1.1 Naming Conventions in Electrochemistry

Note that in electrochemistry, an "anodic current" consists of positive charges flowing from an electrode into the solution. The electrode where this occurs is called the "anode." Similarly, a "cathodic current" is negative charges flowing from the electrode into the solution. Thus negative ions are attracted to the anode, and positive ions to the cathode. The sign of the cathodic current is the same as that of electrical current. In an electrolytic cell where we drive the reaction by applying a current, the anode has a positive potential and the cathode has a negative potential. In other words, the applied current flows from the anode to the cathode.

Instead of referring to the anode and the cathode, we may also speak in terms of the "working" and the "counter" electrodes. The working electrode is where the electrochemical reaction of interest occurs. The counter electrode should essentially just pass current with minimal reaction with the solution.

For ITO reductions, we will apply current from the electrochemically neutral platinum electrode to the ITO electrode. Positively charged sodium ions enter the ITO. Thus, the platinum electrode can be thought of as both the "counter" electrode and the anode, while the ITO is the "working" electrode and the cathode.

2.1.2 Two Electrode Cell

A two electrode cell [55] is the simplest electrochemical cell design, consisting of a working electrode and a counter electrode. We control the amount of current passing through the cell, which, if the reaction is not otherwise limited, controls the difference of the electrode potential from equilibrium and therefore the rate of the reaction. Ideally, both electrodes should have a large enough surface area to not restrict the rate. A basic schematic is shown in Figure 2.

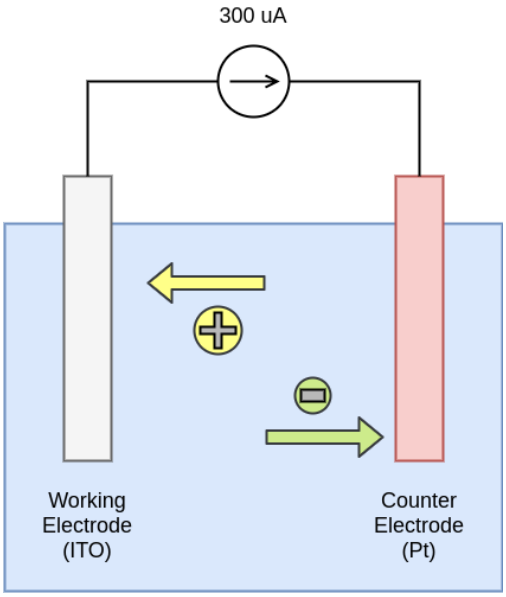

Figure 2: A diagram showing the basic concept of our electrochemical cell with two electrodes. Current is driven from the positively charged (anodic) counter electrode made of platinum to the negatively charged (cathodic) working electrode made of ITO. As a result, the positively charged ions in the solution are attracted to the ITO, while negatively charged ions are attracted to the platinum.

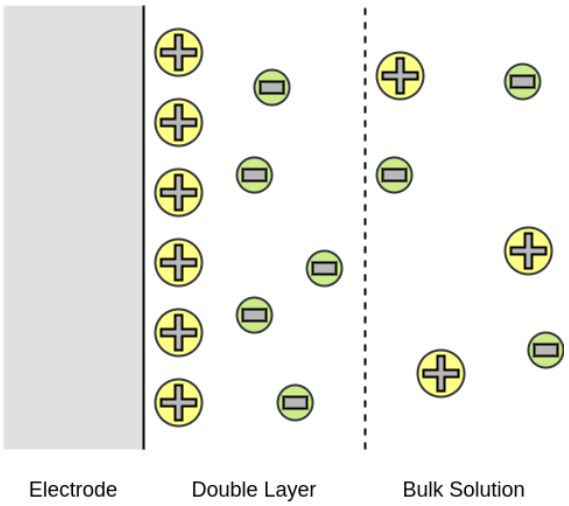

Figure 3: A simplified diagram of a double layer. The double layer forms at the interface between a solid and a solution. One species of ion is preferentially attracted to the surface, and the other species is then attracted to the first layer

However, even in the ideal case, this setup is insufficient to fully determine the potential difference of the electrode from its equilibrium value. Potential does not uniformly drop across the distance between the working electrode and the counter electrode due to the formation of a "double layer" at the interface between a solid and a solution. As shown in Figure 3, one species of ion will be more attracted to the surface of the electrode, resulting in charge buildup.

In the solution near the surface, ions of opposite charge will be more attracted to this region, while ions of the same charge are repulsed. This results in a second "diffuse layer" with a higher concentration of the opposite charge ions. Overall, the double layer is charge neutral, but inside it there is a separation of charge into two layers. Though an imperfect analogy, the double layer is electrostatically similar in some ways to a depletion region in a semiconductor PN junction. To further the analogy, the bulk solution can be compared to a quasi-neutral region, where charges are not separated.

As in semiconductor junctions, the steepest potential drop typically occurs in the double layers. However, unlike semiconductor junctions, charges in the bulk solution are fairly mobile, so appreciable current and voltage do drop in the bulk as well. A rough approximation of a potential diagram for a two-electrode cell is shown in Figure 4.

Some species of ion may adsorb even onto an electrically neutral electrode, but cations like sodium typically do not. Therefore, the double layer at the ITO electrode will effectively be set

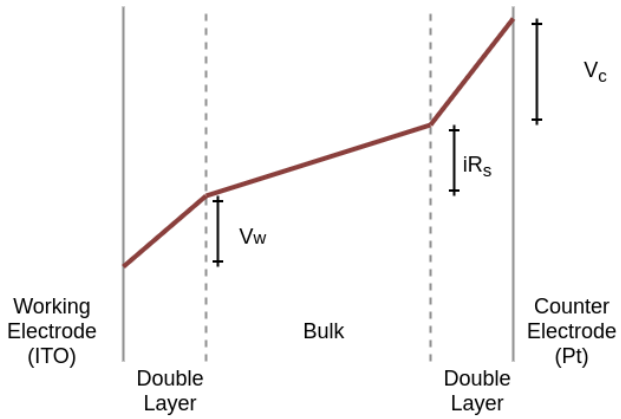

Figure 4: Schematic showing where potential drops in an electrochemical cell. Most drops in the double layers at each electrode, but there is appreciable potential drop in the bulk solution as well due to the finite resistance.

by the charge we apply to it.

The potential dropped in the double layer is called the "surface overpotential," and is our most direct indication the rate of reaction at the electrode. Although it is partially specified by the applied current and by the current drop between the working and counter electrodes, it cannot be fully measured or controlled in a two electrode cell.

As we can see from Figure 4, the total potential difference between the working electrode and counter electrode is the sum of the potential drop in each double layer as well as the potential drop in the bulk due to current times the solution resistance. However, we really want to know the surface overpotential dropped in just the working electrode double layer. To measure the surface overpotential, we will need a different cell architecture.

2.1.3 Three Electrode Cell

The primary complicating factors for measuring surface overpotential in the two electrode cell are the unknown potentials at the surface of the counter electrode and dropped across the electrolyte solution. If we add a reference electrode through which negligible current passes, we can instead measure the potential difference between it and the working electrode, assuming the reference electrode is approximately at equilibrium with the solution. Ideally we would make a reference electrode out of a material that will not interact with our solution, and which is protected from stray currents. Lacking that, we can instead use another piece of our working electrode mate-

rial. Since we will not be using the surface overpotential to perform quantitative electrochemical measurements but rather as an indicator variable, this approximation will be sufficiently accurate.

Our metric for surface overpotential will then be the potential difference between the working electrode ITO and a piece of ITO in equilibrium with the solution. A schematic for such a cell is shown in Figure 5.

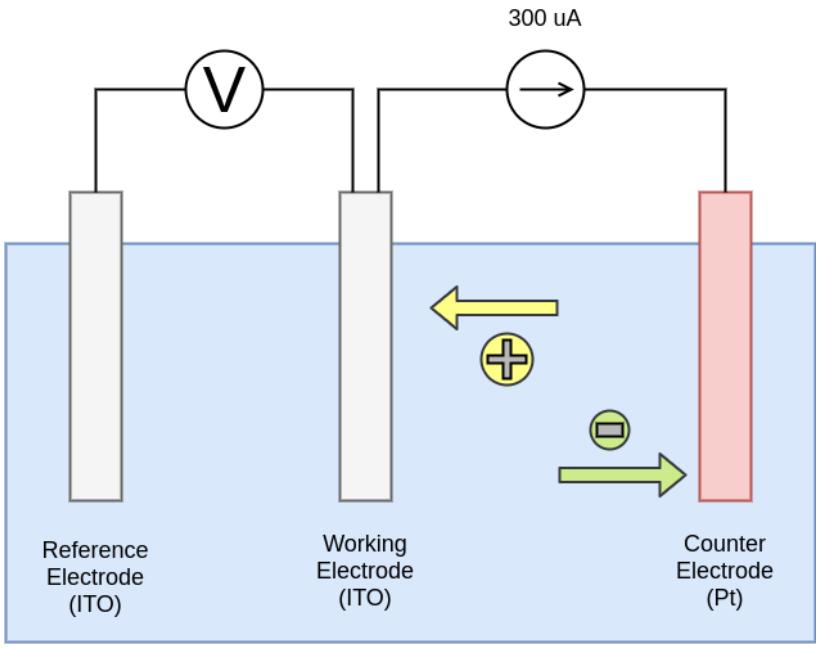

Figure 5: A diagram showing the basic concept of our electrochemical cell with three electrodes. Current is driven from the positively charged (anodic) counter electrode made of platinum to the negatively charged (cathodic) working electrode made of ITO. An additional ITO electrode which is roughly in equilibrium with the solution is used as a voltage reference. Approximately no current flows between the reference and other electrodes.

Current dynamics in the electrochemical cell can also have significant impact on the reduced material, so we developed an apparatus to hold the three electrodes at consistent distances and orientations across many reductions. Machining details for this apparatus are given in Appendix A. The apparatus, resting on top of the beaker in which the electrochemical reactions occur, is shown in Figure 6.

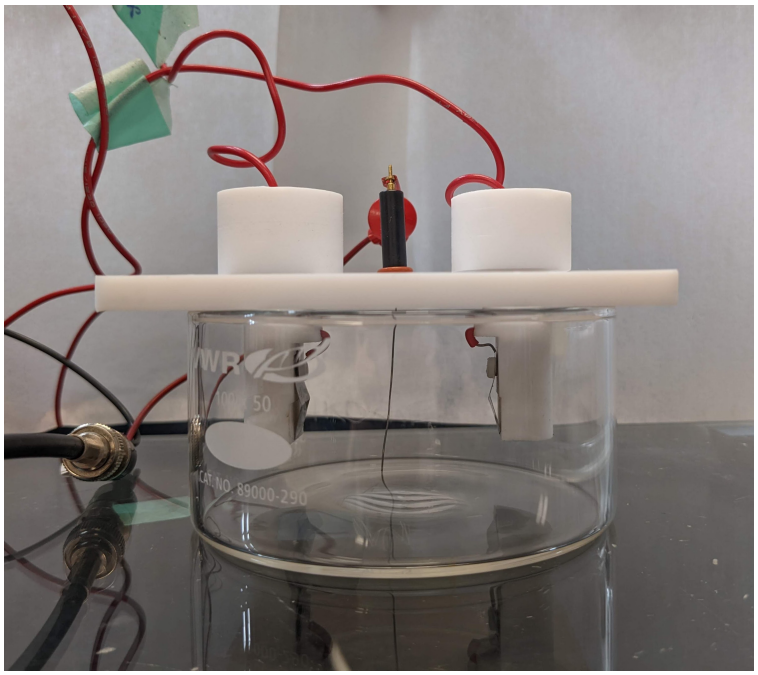

Figure 6: The completed electrochemical cell apparatus. The ITO sample holders to the left and right are symmetric, so the reference versus working roles are set by the electrical wiring. The platinum counter-electrode rests in the center.

2.1.4 Galvanostatic Reduction Process

Following Aliev et al.[7], we controlled the flow of electrons with applied current and measured the resulting induced voltage. In electrochemistry, this is referred to as a galvanostatic method or controlled-current chronopotentiometry. We briefly compared this method to a controlled-voltage method, but found our cell was more difficult to control in this fashion.

At small applied currents and short amounts of time, the reduced ITO quickly changes color, enough that the researcher can watch in real time as the submerged film transitions from almost perfectly clear, to translucent reddish brown, to a metallic, almost purple gray-brown shine. These color changes were well-correlated with other electronic behaviors of the film and thus extremely useful as an in situ diagnostic tool. The films appeared nearly fully metallic after just five minutes at 300 μA. For a film with about half a square centimeter exposed to electrolyte, 120 seconds at 300 μA results in a translucent brown film with little metallic character, such as the sample shown in Figure 7. This corresponds to a reduction charge density of about 75 mC/cm^2. Many of our reductions targeted this intermediate reduction amount, as early signs hinted at and rigorous experiments later confirmed it tends to produce the highest transition temperatures.

Figure 7: A photograph of ITO on glass, the lower half of which was exposed to about 75 $\mathrm{mC/cm^2}$ reduction charge density.

2.1.5 Methodology and Instrumentation

All reductions followed the same general process to ensure reproducibility of results. First, sample pieces are cut into a suitable shape for the electrochemical cell. For ITO on silicon, we diced the wafers into 2 cm x 1 cm pieces on a diesaw. For ITO on glass slides, we scored the backs of the slides with a glass cutter and cleaved them into pieces, aiming for roughly a 2:1 ratio. The pieces are then sonicated for five minutes in acetone and five minutes in IPA. Samples intended for microelectronics patterning may additionally need to be plasma-cleaned to ensure removal of all organics from the surface; however, work for this thesis involved sufficiently large feature sizes that we found this step unnecessary. Clean samples are stored in nitrogen until reduction.

For current control, we used a Hewlett-Packard 6177C DC current source. It has an analog dial, so we added a Keithley 6485 picoammeter in series to measure its output so we could set and monitor the current with greater precision. The positive current lead was attached to the platinum counter electrode; the negative lead to the ITO working electrode. The potential difference between the working electrode and the ITO reference electrode was measured with a NIST digital acquisition device model USB-6215. With the ITO pieces fixed in place in our electrochemical cell, generally between a quarter to a half of the height of each piece was submerged in electrolyte.

As a result each piece could undergo two unique reductions, one on each half.

The length of time of the reduction is defined as the time that passes between turning on the current source and turning it back off. Especially after the current source is first turned on, the electrochemical cell requires a few seconds to stabilize to and maintain a particular current value. New electrolyte was obtained from a source jug of 1 M saltwater between each reduction to avoid buildup of side products from the reduction in solution. The pH of this solution was found to be slightly acidic, around a pH of 5, but stable.

Once the reduction is complete, samples were immediately rinsed with deionized water and dried in nitrogen. Sometimes samples were then annealed at 160 $^{\circ}\mathrm{C}$ for one hour, as done by Aliev et al. [7], but this was not found to much affect the resulting film. After this step, samples were ready for whatever further analysis or processing might be required.

2.2 Material Characterization

In addition to the electrochemical processing, we also used a number of techniques for characterizing the resulting materials. To perform this characterization, we reduced many different samples to different reduction charge densities. Any given sample section was always reduced in one step to a single reduction charge density, because we found it difficult to get a uniform reduction upon multiple reductions of a single sample. If the sample was removed from the solution, saltwater would drip and dry in nonuniform ways, and another full cleaning would have been required to make the surface uniform again. Therefore, samples with a unique reduction amount are simply referred to by either their reduction time or their reduction charge density; samples that share a reduction amount with other samples are additionally specified by letters following the reduction quantity.

This work was carried out on ITO parent material from several different sources. Most of the electronic and composition work was done on ITO on glass slides from Sigma Aldrich, which we will refer to as "ITO on glass"; most of the optical and structural work was done on ITO sputtered onto two silicon wafers by the Bulovic group at MIT, which we will refer to as "ITO on silicon." Some preliminary testing with promising results was also done with ITO epitaxially grown on yttrium-stabilized zirconium by the Mundy group at Harvard, but we did not examine it in a systematic way in this work. Note that despite our shorthand, it is not only the substrates that differ

but also the deposition process and therefore possibly the carrier concentration, transparency, crystallinity, sheet resistance, and so on. Therefore our characterizations must all be understood as changes induced by reduction relative to the particular parent material, not in absolute terms.

The relevant material properties can be split into three essential categories: electronic properties, material structure and composition, and optical properties. In the following sections, we will describe the methods used to explore each of these categories.

2.2.1 Electronic Properties

Perhaps the most fundamental task for developing a material for use in superconducting electronics is to establish its electronic properties, namely room-temperature resistance and transition temperature. Room-temperature resistance is related to other key properties, such as carrier concentration, carrier mobility, and, in superconductors, kinetic inductance. Meanwhile, the transition temperature of the material determines what operating temperatures might be suitable, as typically superconducting devices work best well below the transition temperature.

Most resistivity measurements were carried out in a four-point probe configuration, which eliminates contact resistance and allows us to see truly zero resistance when the film is superconducting. Room-temperature measurements were performed with a pogo pin 4-point configuration and a Keithley source-meter. The transition temperature was determined by wirebonding into a 4-point configuration onto the sample and measuring resistivity as the sample was warmed or cooled through its superconducting transition. Some measurements were performed in the ICE-Oxford fridge, which can cool down to 1 K; others were performed in a 300 mK fridge. Most samples exhibited superconducting transitions above 1 K.

2.2.2 Structure and Composition

To understand reduced ITO, we had to determine the structural changes to the films as well as the doping mechanism. Structural changes were observed with SEM and STEM imaging of both the film surfaces and film cross-sections. Compositional changes were determined through a combination of energy-dispersive x-ray spectroscopy (STEM-EDS) and x-ray photoelectron spectroscopy (XPS). We will describe the fundamentals of these techniques here.

Energy-dispersive x-ray spectroscopy (STEM-EDS) is an effective tool for simultaneously

measuring material composition as a function of depth while capturing a corresponding image of the area [56]. It is also, notably, a non-destructive technique, so further analysis can be performed on samples used with STEM-EDS, particularly other STEM techniques.

The STEM electron beam can be used at a high enough energy to eject core-shell electrons as it is scanned across the sample. Higher-energy outer-shell electrons will drop down to take the place of the ejected electrons, resulting in X-ray emissions that can be traced back to a specific positions on the film. The energies of the X-ray emissions are measured, and the associated electron binding energies are computed by subtracting the X-ray emission energy from the electron beam energy. Different species of atoms are associated with different binding energy spectra. Thus the position-dependent x-ray spectra can be interpreted as position-dependent compositional data.

The major limitation of STEM-EDS is that the high-energy electron beam penetrates deep into a film, so for accurate measurements we must prepare a very thin ($\tilde{1}$00 nm thick) lamella from our sample and attach it free-hanging from a mount. The sample preparation process is therefore very involved and cannot be performed on a large number of samples. Also, energy resolution for STEM-EDS is rather poor, it is not a very quantitative measurement, and it is not very suitable for detecting lightweight elements such as oxygen.

X-ray photoelectron spectroscopy (XPS) [57] operates on a similar principle as EDS, but uses x-ray photons instead of a high-energy electron beam to eject electrons from the core shells of atoms. These x-ray photons typically only penetrate a few nanometers into any given material, so XPS is considered a surface analysis technique. Also, XPS can measure energy spectra with extremely high resolution, and as a result can distinguish not only different atomic species but even different chemical bonding states of a single atom.

XPS surface analysis can be performed relatively quickly on several samples with minimal preparation, although obtaining quality, high-resolution spectra can still be time consuming. Additionally, a depth-dependent composition profile can be obtained by sputtering the film under analysis with either inert gas ion beams such as argon or cluster ion beams such as buckyballs. This technique, called depth profiling, is a destructive analysis method, but only consumes a small area of film, so other parts of the sample can be further analyzed.

Making use of both STEM-EDS and XPS will give us a great deal of information about the composition and chemical bonding states of our films and allow us to correlate that compositional

information with film morphology and depth.

2.2.3 Optical Properties

Finally, in order to evaluate reduced ITO as a transparent superconductor, we must be able to quantify its optical properties. Our primary tool for this will be variable-angle spectral ellipsometry (VASE) [58], which leverages the way materials interact with polarized light in order to simultaneously extract the thickness and optical constants of these materials. Here we will give a brief derivation of this interaction.

In a variable-angle spectral ellipsometer, light at many different wavelengths at a known polarization shines onto the sample at a controllable angle θ. Any polarization of light can be written as a superposition of parallel and perpendicular polarizations, and typical materials will reflect parallel polarizations differently than perpendicular polarizations. Therefore we define the Fresnel reflection coefficients to help quantify this effect in equations 34, where the subscript p denotes the parallel polarized component and s the perpendicular polarized component. In these equations, E_{refl} is the amplitude of the reflected light and E_{inc} is the amplitude of the incident light.

$$r_p = \frac{E_{\text{refl},p}}{E_{\text{inc},p}} \qquad\qquad r_s = \frac{E_{\text{refl},s}}{E_{\text{inc},s}} \tag{34}$$

Now let us generalize to a system with some number of homogeneous, isotropic thin films each with their own refractive indices and thicknesses between the air on top and the substrate at the bottom. According to Snell's law, the Fresnel reflection coefficients of the j^{th} layer can be rewritten in terms of the incident angle θ and the complex refractive index $\tilde{n} = n + k$, as shown in equation 35.

$$r_{jp} = \frac{\tilde{n}_j \cos\theta_{j-1} - \tilde{n}_{j-1} \cos\theta_j}{\tilde{n}_j \cos\theta_{j-1} + \tilde{n}_{j-1} \cos\theta_j} \tag{35}$$

From the Fresnel reflection coefficients we can define reflection matrices I_j and the transfer matrix L_j for the j^{th} interface, given in equation 36:

$$I_{jp} = \begin{bmatrix} 1 & r_{jp} \\ r_{jp} & 1 \end{bmatrix} \qquad I_{js} = \begin{bmatrix} 1 & r_{js} \\ r_{js} & 1 \end{bmatrix} \qquad L_j = \begin{bmatrix} e^{i\delta_j} & 0 \\ 0 & e^{-i\delta_j} \end{bmatrix} \tag{36}$$

where $\delta_j = \frac{2\pi}{\lambda}\tilde{n}_j d_j \cos\theta_j$ is the phase added by traveling through the thickness d_j of the layer. The total scattering matrices of the whole structure are defined in equation 37:

$$S_p = \left(\Pi_{j=1}^{N} I_{jp} L_j\right) I_{(N+1)p} \qquad S_s = \left(\Pi_{j=1}^{N} I_{js} L_j\right) I_{(N+1)s} \tag{37}$$

where N is the total number of layers in the structure. The effective reflection coefficients can be expressed in terms of these scattering matrices, as in equation 38.

$$R_p = \frac{S_{21,p}}{S_{11,p}} \qquad R_s = \frac{S_{21,s}}{S_{11,s}} \tag{38}$$

Crucially, the complex ratio of these reflection coefficients can be directly measured, allowing us to finally relate the refractive indices and thicknesses of the layers to an observable quantity. This ratio is usually reported in terms of real quantities Ψ and Δ, which are related to the reflection coefficients in equation 39.

$$\rho = \frac{R_p}{R_s} = \tan\Psi e^{i\Delta} \tag{39}$$

However, the relationship between Ψ, Δ, the refractive indices, and thicknesses of the layers is not trivial. There may even be multiple solutions for refractive index and thickness combinations that can yield the same Ψ and Δ. We address this problem first by collecting a lot of data, at many different wavelengths and angles, to decrease the number of reasonable solutions. Secondly, we model the optical constants as physically-justified functions of photon energy with material-different fitting parameters, rather than trying to backcompute the optical constants at each wavelength independently.

The simplest of these functions are called dispersion laws, and they are suitable for the homo-

geneous, isotropic thin films assumed earlier in our derivation. Issues like surface roughness can be addressed with more advanced analysis techniques such as the effective medium approximation. By choosing appropriate models for the reduced ITO system, we will be able to accurately extract its optical constants and thickness from ellipsometric measurements.

To perform the ellipsometric measurements, we used a variable-angle spectral ellipsometer (VASE) from Semilab, the Semilab SE-2000 spectroscopic ellipsometer. Inclusion of many wavelengths and several angles provides more data, allowing for an improved fit. For all samples, we took measurements at $60°$, $65°$, and $70°$ or $65°$, $70°$, and $75°$ at over 1000 wavelengths between $240\,\mathrm{nm} - 1700\,\mathrm{nm}$. Data from all angles and wavelengths for a given sample were fit simultaneously.

3 Structure, Composition, and Electronic Properties of Reduced ITO

Simply put, we hope that electrochemical reduction of ITO will increase carrier concentration of the film while preserving the properties that make ITO suitable for electronics, such as high conductivity and transparency. In order to make high-carrier-concentration, high quality films of reduced ITO, it will be critical to understand the way reduction affects the structure and composition alongside the electronic properties of ITO films. Over the course of our experiments, we observed surprisingly rich and strange behaviors, with significant implications for the performance of reduced ITO electronics and future directions for its research. In the following section, we will confirm that our process generates superconducting ITO films and discuss the physical and chemical effects of reduction on ITO films.

3.1 Electronic Properties of Reduced ITO

Before we can study reduced ITO as a transparent superconductor we must first confirm that it indeed superconducts. Previous work indicates that ITO can have a transition temperature as high as 5 K [7], but typically the transition temperature is lower [32, 6, 34]. In addition to confirming superconductivity, we should also confirm the dome-shaped dependence of transition temperature on carrier concentration and determine the maximum possible transition temperature. For our experiments, we will use reduction charge density as a proxy variable for carrier concentration.

First we explore how the room-temperature sheet resistance changes with reduction time, as this can help us understand how carrier concentration and mobility might be changing. Also, room-temperature sheet resistance is an important predictor of superconducting kinetic inductance, a key property for electronic design. We took five pieces of ITO on glass and ITO on silicon and reduced each half for 60 s, 90 s, 120 s, 150 s, or 180 s. Because of the design of the electrochemical cell, the ITO on silicon samples all had about 0.5 cm x 1 cm exposed to reduction current. However, the ITO on glass samples varied somewhat in shape, so different areas were exposed to reduction current. Therefore we report our results in terms of reduction charge density for easier

comparsion.

Notably, we observed different effects of reduction on sheet resistance depending on our starting material. For ITO on silicon, sheet resistance universally decreased with reduction, as shown in Table 1. However, the final sheet resistance is basically independent of reduction charge density or original resistance. For ITO on glass, sheet resistance increased with reduction charge density, as shown in Table 2. It is unclear why the two types of films perform differently.

Reduction Charge Density [mC/cm^2]	Original $R_s[\Omega]$	New $R_s[\Omega]$	Percent Change in $R_s[\Omega]$
36 (a)	50	43	-13%
36 (b)	50	44	-12%
54 (a)	58	40	-30%
54 (b)	58	38	-34%
72 (a)	42	38	-8%
72 (b)	42	40	-4%
90 (a)	47	39	-17%
90 (b)	47	46	-1%
108 (a)	46	41	-11%
108 (b)	46	41	-11%

Table 1: Sheet resistances before and after reduction for ITO sputtered onto silicon. Final resistance is basically independent of reduction charge density.

Reduction Charge Density [mC/cm^2]	Original $R_s[\Omega]$	New $R_s[\Omega]$	Percent Change in $R_s[\Omega]$
16	11	12	9%
19	11	12	9%
30	9	13	48%
41	9	14	54%
54	12	17	38%
55	12	17	40%
63	11	15	41%
80	11	19	77%
91	12	91	317%
130	12	32	162%

Table 2: Sheet resistance before and after reduction for ITO on glass from Sigma Aldrich. Increasing reduction charge density correlates with an increase in sheet resistance.

The decreases in resistance seen in ITO on silicon is likely due to the increased carrier concentration. The mobility for the original film was probably not optimized, so any decrease in mobility from lattice defects or strain from the doping process are more than made up for by the increase in carriers. Meanwhile the increase in resistance seen in ITO on glass is actually in line with reports from others who reduced commercially-obtained ITO [7]. Given the very low starting sheet resistance values of the ITO on glass, it is possible that the ITO on glass deposition process was optimized to minimize the sheet resistance. The mobility of the parent film was probably very high, and could be significantly decreased by doping, leading to a net increase in sheet resistance despite the added carriers. Note that for the most part the final sheet resistance for ITO on glass is still lower than that for ITO on silicon. In any case, the indications of electronic changes are promising, but for our purposes the most important electronic property is superconductivity. We measured the transition temperature for a number of samples, both on silicon and on glass.

At first, working with the ITO on silicon, we found it difficult to achieve reproducible transition temperatures. This is primarily because reduction charge density, although convenient and easy to measure, is not a fully explanatory independent variable. During our initial transition temperature measurements, for instance, we used ITO from a different wafer than for the resistance measurements cited earlier. The original sheet resistance of samples from that wafer varied from $210\,\Omega - 380\,\Omega$ – very high and also highly variable, compared to the later wafer with variations from $42\,\Omega - 58\,\Omega$. The two wafers may have had different initial carrier concentrations, meaning that the same reduction charge density would lead to different final carrier concentrations.

Additionally, when we were developing the electrochemical apparatus, we noticed that different loads from the readout electronics led to different rates of color change, and likely change in electronic properties too. When we used a Keithley source-meter for current control and voltage readout, we saw different results than with an oscilloscope for readout, or than with our final configuration using a NIST DAQ for readout. Comparing the voltages, these different configurations also caused different levels of surface overpotential. So the total reduction power may have some impact on the actual reduction charge inserted into the film as well, or perhaps non-ideal voltage measurement devices siphon different amounts of leakage current away from the electrochemical cell.

However, by settling on a specific configuration and using less variable intial ITO, we were able to solve the reproducibility issues, and reduction charge density again became a simple and predictive variable. We measured the transition temperatures of several ITO on glass samples, as well as a control sample that had not been reduced. The superconducting transitions, shown in Figure 8, were fairly narrow for such an unusual material, and we were able to reproduce the dome-shaped dependence of transition temperature on reduction amount. The highest transition temperature we achieved was 4.1 K in a film reduced to $59\,\mathrm{mC/cm^2}$. Transition temperatures up to 3.6 K were observed in ITO on silicon, but this was on the high-resistance wafer and before the electrochemical readout was finalized, so reduction charge density is not a suitable comparison.

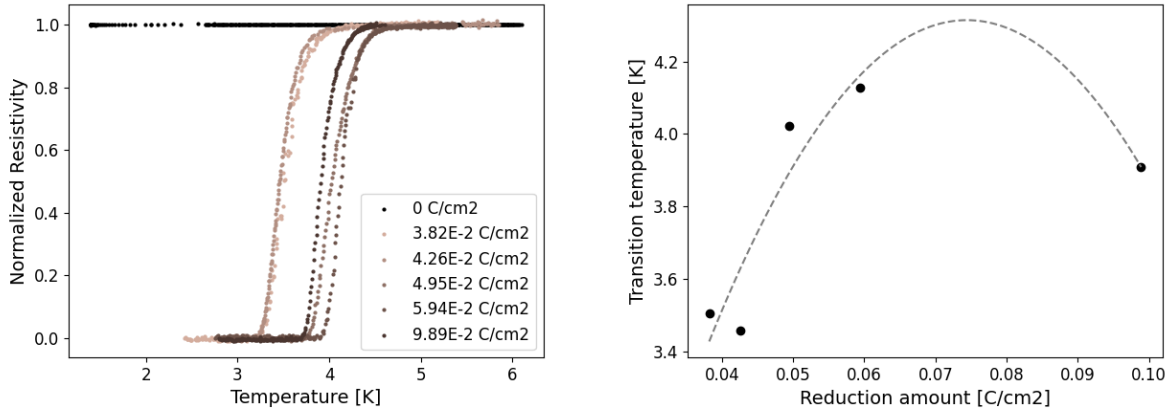

(a) (b)

Figure 8: (Left) Superconducting transitions for ITO on glass films reduced to varying charge densities and (right) the dependence of transition temperature on total reduction charge density. The transition shape is reasonably sharp, and we observe a dome-shaped dependence of transition temperature on reduction charge density.

In all, the electronic data we collected indicates promise for ITO as a transparent superconductor. The transition temperatures achieved are high enough for operation of electronics in standard cryogenic set-ups and are reproducible once factors like initial carrier concentration are controlled for.

3.2 Surface Morphology: Nanoparticle Formation

Invariably in our experiments, we found that electrochemical reduction was accompanied by formation of nanoparticles on the surface of the film. These nanoparticles are generally ellipsoidal,

seemingly randomly distributed, and sharply localized to regions of the film that were directly exposed to a reducing current. A typical example of a reduced ITO surface is shown in Figure 9.

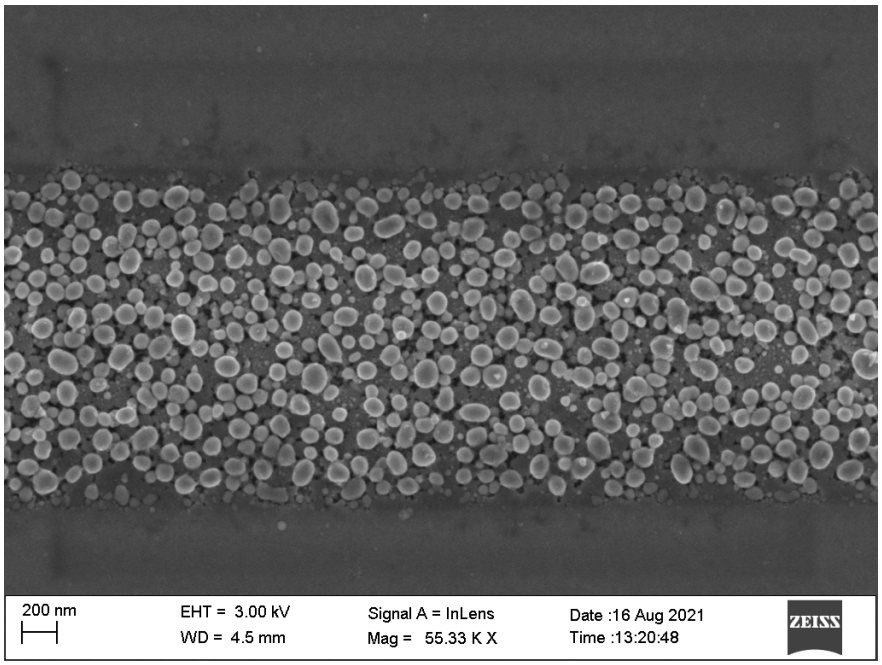

Figure 9: SEM of nanoparticles on a microwire of reduced ITO on silicon. The surrounding ITO was masked with S1813 during reduction and not directly exposed to current; the wire was designed to be 2 microm wide and measures 1.9 microm wide. The nanoparticles are generally ellipsoidal, seemingly randomly distributed, and sharply localized to the exposed parts of the film. Reduction was performed with 95 μA of current for 50 s over an exposed area of 6.6×10-2cm^2, totaling about 72 mC/cm^2.

The particles come in roughly two size regimes, having either a diameter of about 100 nm or greater or a diameter of about 10 nm or less, with few particles of intermediate sizes. Cross-sectional SEM indicates that these nanoparticles form on top of the original surface of the ITO as shown in Figure 10, and later we will show this result is corroborated by S/TEM with EDS and ellipsometric data as well. Also note that the smallest nanoparticles are primarily observed closest to the original surface of the ITO, while the larger nanoparticles are piled on top of this new fine nanoparticle surface and each other.

Several other authors have also observed surface nanostructures after reduction of ITO under a wide range of conditions, including reduction by hydrogen plasma [59] or forming gas [60], and electrochemical reduction in acetonitrile with sodium iodide [61] or in electrolytes of varying pH

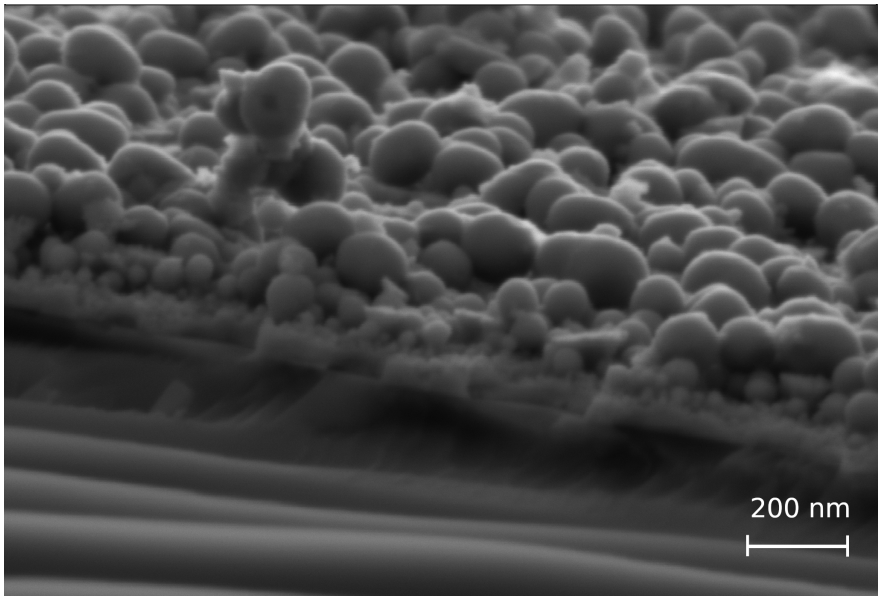

Figure 10: SEM Cross-section of nanoparticles on a thin film of reduced ITO on silicon. Observe the different strata along the cleaved edge: the smooth, light gray layer of the original ITO film transitions into a layer of very small nanoparticles, and the larger nanoparticles that are so striking from a top-down view rest on top of that layer.

with different salts of potassium [62]. Across these papers, we observe that the exact morphology of the nanoparticles is highly dependent on both reduction conditions and the properties of the underlying ITO. Fan et al. found that nanoparticle growth is slower and more uniform on polycrystalline ITO compared to amorphous ITO [59]. They also proposed an explanation for the formation dynamics of the nanoparticles. They suggest that reduction of the oxide releases metallic ions from the surface of the film, which then nucleate and grow according to a Volmer-Weber mode of film growth, where the metallic ions are more attracted to themselves than the surface and therefore form islands instead of a uniform film [63].

Similarly, our samples exhibit different nanoparticle morphologies depending on primarily the initial material properties and total reduction charge. For instance, Figure 11 shows cross-sectional SEMs of two samples. The sample on the left was reduced less, for 150 s to a total of about 90 mC/cm^2, while the sample on the right was reduced for 180 s to about 108 mC/cm^2. The less-reduced sample exhibits smaller, more uniform nanoparticles. In the more-reduced sample, we still see a uniform distribution of these smaller nanoparticles, but now with larger nanoparticles piled on top. Seemingly, the diameter of the largest nanoparticle increases with reduction amount, but smaller nanoparticles are not totally consumed during their formation.

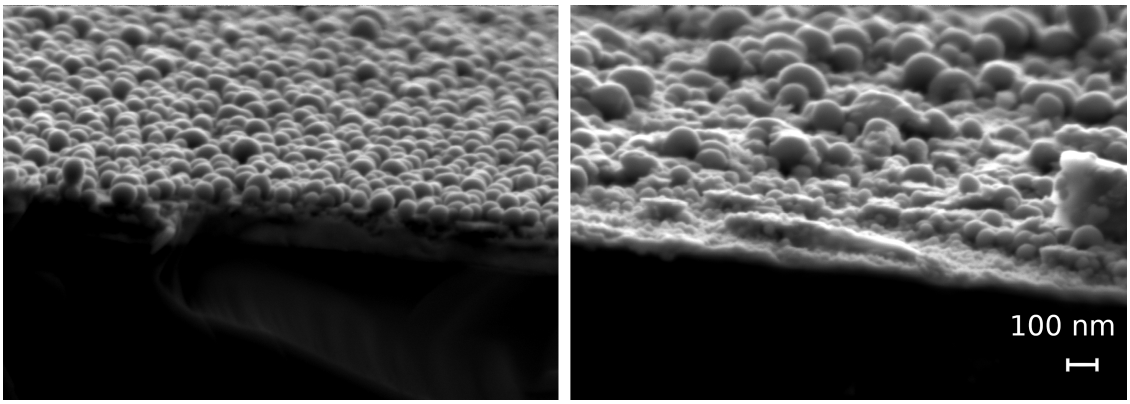

Figure 11: Cross-sectional SEM of ITO on silicon samples reduced by different amounts. (Left) Sample reduced to 90 mC/cm^2, with small nanoparticles of uniform size. (Right) Sample reduced to 108 mC/cm^2, with sparse formation of larger nanoparticles on top of particles similarly sized as the other sample. Brightness/contrast adjusted in GIMP so all levels were similar.

We took additional top-down SEMs of samples reduced for 60 s, 120 s, 150 s, and 180 s for further comparison, corresponding to reduction charge densities of $36\,\mathrm{mC/cm^2}$, $72\,\mathrm{mC/cm^2}$, $90\,\mathrm{mC/cm^2}$, and $108\,\mathrm{mC/cm^2}$. These images are shown in Figure 12. The least-reduced sample exhibits a markedly different morphology than the others, with only a very sparse layer of nanoparticles. However, by a reduction charge density of $72\,\mathrm{mC/cm^2}$, the nanoparticle layer has already become dense and uniform. Despite the striking differences between the cross-sections of the more-reduced films, they are nearly indistinguishable from the top-down point of view. The layer reduced to $72\,\mathrm{mC/cm^2}$ seems to be thinner or sparser, allowing us to see more of the smaller, lower-level particles in between the upper nanoparticle layer. Otherwise there are no obvious visual distinctions. The cross-section is a better tool for studying the evolution of nanoparticle morphology.

We also explored how higher-temperature annealing could affect the nanoparticle layer. We chose $250\,^\circ\mathrm{C}$ because it is reasonably well above the melting point of indium and tin and annealed in air a sample which had been reduced for 120 s for about half an hour. Afterward, transparency was almost fully restored and, as seen in the SEM in Figure 13, the nanoparticles were still present but some showed odd rifts across their surfaces, perhaps indicating combination of nanoparticles at this temperature. In any case, the restoration of transparency without very significant structural changes are strongly indicative that the optical properties are more related to compositional

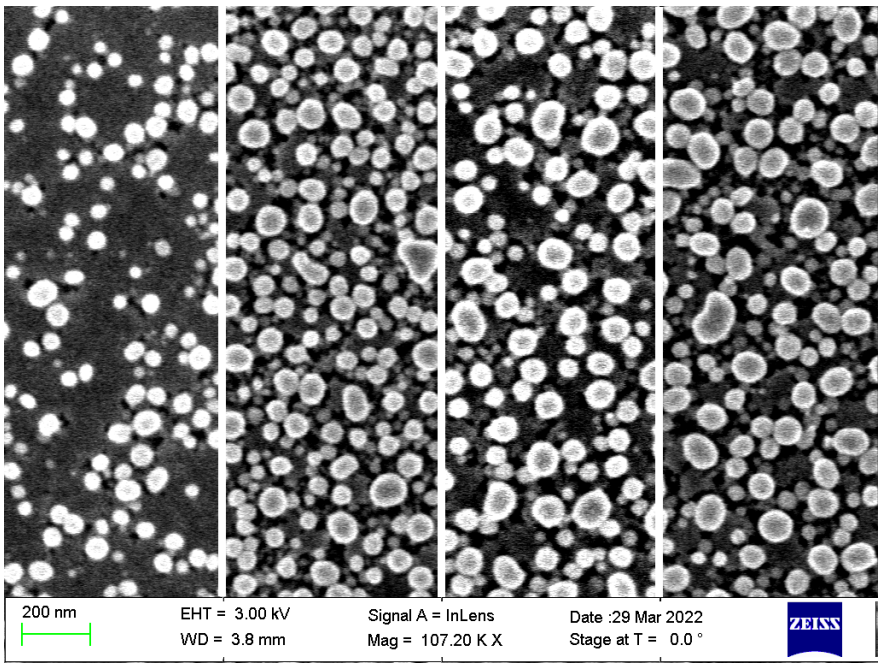

Figure 12: Top-down SEM of ITO on silicon samples reduced by different amounts. Left to right: 60 s, 120 s, 150 s, 180 s. Although a marked difference was discernible in the cross-sectional images for samples at 150 s and 180 s, they look similar from the top view. However, the sample reduced for 60 s exhibits a much sparser film than more-reduced samples. Brightness/contrast adjusted in GIMP so all levels were similar.

changes rather than the nanoparticle structure.

The thickness of the nanoparticle layer is significant compared to the thickness of the original film. In the above SEM images, we consistently observe a uniform coating of nanoparticles about 100 nm in diameter, on top of a film that was originally about 130 nm thick. It stands to reason, then, that the properties of the nanoparticles will contribute significantly to the properties of reduced ITO films, so we must study them carefully.

3.3 Doping Mechanism

Previous sources have proposed sodium intercalation as the primary doping mechanism for ITO reduced in sodium salts, and supported these claims with XRD [7] and XPS [61] measurements.

However, other authors who observed electrochromism in ITO debated whether ion intercalation occurs in ITO at all [64]. Additionally, the changes Aliev eta al. observed in the XRD patterns are similar to those attributed to presence of metallic indium elsewhere in the literature

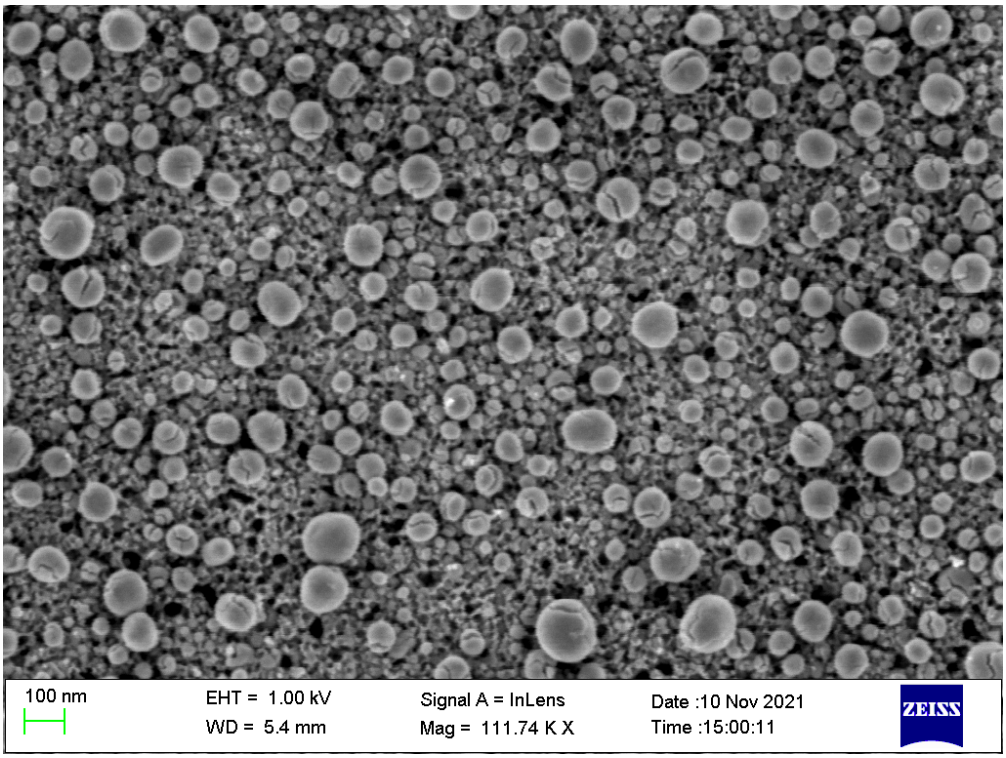

Figure 13: SEM of nanoparticles on a sample reduced for 120 s and then annealed in air at 250 °C for 30 minutes. The cracks through some of the centers may be evidence of nanoparticle combination.

[62]. After all, XRD patterns measure structural changes, not compositional ones. These patterns are the only direct evidence of sodium ion intercalation in the work of Aliev et al., whose reduction methods are most similar to ours and whose films are confirmed to superconduct.

The XPS data from the work of Bouden et al. seems to be a more straightforward indicator of sodium presence in the film, but it is worth noting that they cite reduction charge densities tens to hundreds of times greater than ours, reporting no results at less than 400 mC/cm^2, and considerably larger nanoparticles. It is quite possible that different behaviors arise at these levels of reduction. Transition temperatures are not reported for their highly reduced films, so it is unknown whether they even superconduct.

Furthermore, the increase in film thickness, observed both in our results and by Bouden et al., has also been reported in films reduced in forming gas, which certainly experience oxygen removal and not ion implantation [65]. Though models show that ion intercalation can, naturally, increase the lattice constant, so too can removal of oxygen. The presence of excess oxygen naturally found in ITO compensates for repulsion between effectively positively charged tin ions;

after its removal, the tin ions push the lattice apart a little more.[66] Interestingly, both ion intercalation and additional oxygen defects are proposed to target 16c lattice sites. In other words, oxygen defects could inhibit ion intercalation until after the excess oxygen is removed.

On the other hand, Liu et al. propose oxygen vacancies as the primary doping mechanism for their electrochemically reduced ITO [62]. This claim is supported by high-resolution XPS peaks showing shifts in the ratios of metallic to oxidized indium and tin at different reduction levels. Additionally, low-oxygen ITO has previously been shown to superconduct [6].

To confirm whether our reduced ITO films have had oxygen removed, we compared results from STEM-EDS data and XPS surface spectra and depth profiles for several films at different levels of reduction.

3.3.1 STEM-EDS Data

Let us first consider the STEM-EDS data. STEM-EDS was performed on a lamella about 100 nm thick prepared from a sample of ITO on silicon which had been reduced for 120 s. Given the reduction area, this corresponds to a reduction charge density of about $75\,\mathrm{mC/cm^2}$. Ellipsometric modeling, which we will discuss in further detail later, indicated a nanoparticle film thickness of about 30 nm. This sample was confirmed to superconduct with a transition temperature of about 3.1 K.

As shown in Figure 14, we can directly compare a cross-sectional image created by transmitted electrons scattered by the material into the high-angle annular dark field (HAADF) with the depth-dependent intensity of x-ray counts associated with different atomic fingerprints. The film is oriented sideways, with the deepest part at the furthest left. We notice there are four distinct regions over the depth, from left to right: the silicon wafer, the primary mass of indium tin oxide, a muddled nanostructured layer with some clear indium and tin content into which the gold and platinum cap has permeated, and the gold and platinum cap. The wafer and the cap are not of much interest, but we can analyze the two ITO layers in more detail.

First, let us consider the primary ITO layer. Deep within this layer, near the silicon wafer, it appears quite uniform. Different orientations of stripey interference patterns indicate a typical polycrystalline film. However, about halfway to the film surface, strange voids begin to appear at random. Some of these voids are filled with a fine texture of nanospheres.

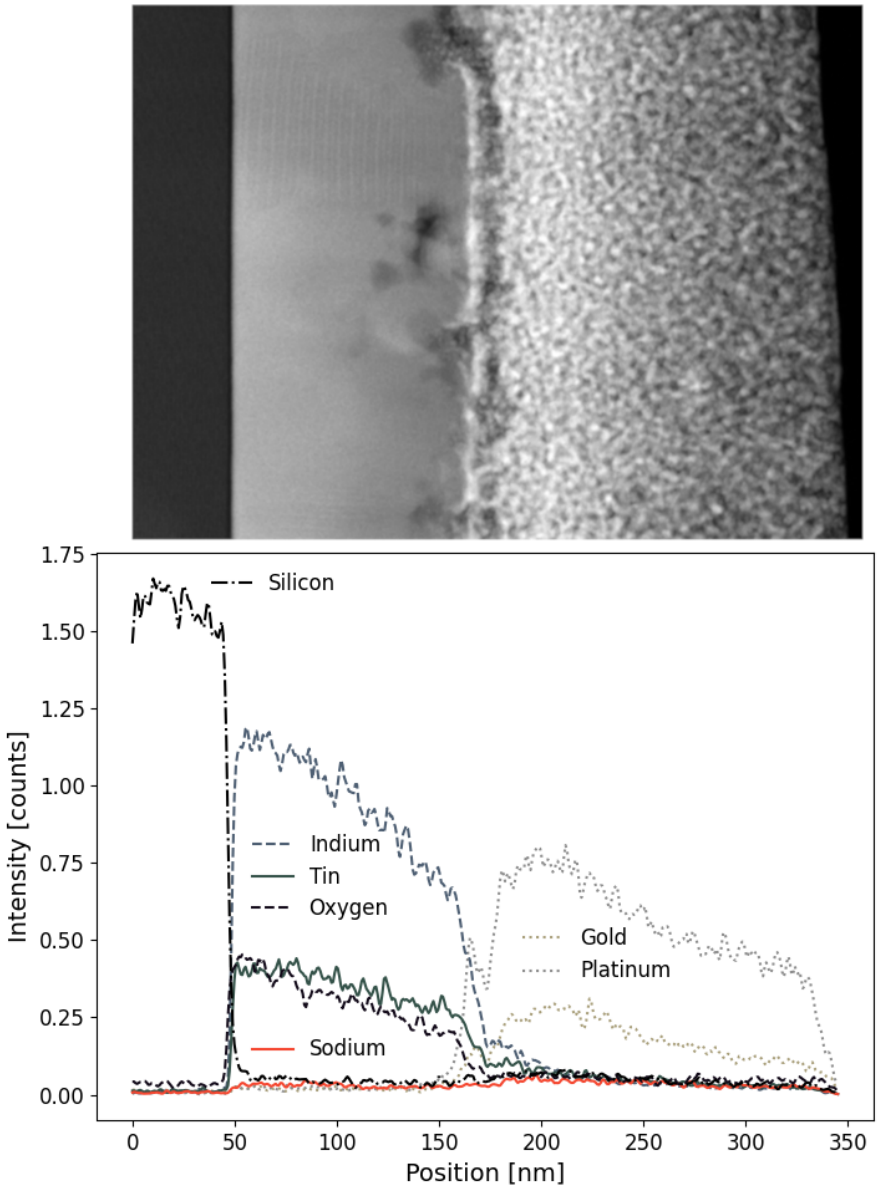

Figure 14: A thin cross-section of ITO reduced for 120 s to about $75\,\mathrm{mC/cm^2}$ imaged with STEM and EDS. The top STEM image shows high-angle annular dark field electrons (HAADF), so brighter regions indicate more electron interaction: that is, denser or more metallic regions. Note different densities and orientations of stripes within the middle ITO section, indicating a polycrystalline film. This region also exhibits odd nanotextured voids, perhaps where ITO was removed by reduction to reform as nanoparticles. The bottom plot shows EDS intensity counts corresponding to this area. The silicon wafer ends sharply about 50 nm into the image, followed by ITO, the density of which apparently decreases towards its surface. After about 150 nm the gold and platinum cap is mixed with the ITO, perhaps falling between the nanoparticles. 200 nm in the indium and tin fall off completely; the nanoparticle layer ends. Sodium signal does not rise about noise levels anywhere in the film.

Beyond these voids, the nice, uniform film more or less breaks down entirely. This layer is difficult to interpret as a large amount of gold and platinum have permeated it. Indium, tin, and oxygen content all decrease. The oxygen counts roughly track the tin counts, decreasing perhaps slightly faster, but fall below noise levels midway through this layer. Oxygen is a fairly light atom, and EDS does not detect it as efficiently as heavier metals, so we cannot say whether the drop-off is from general film density decrease or a genuine decrease in oxygen relative to indium and tin from this data alone.

One of the oddest features of this layer is that a bright dense stripe, presenting as many counts from gold and platinum as from indium and tin, seems to lie below a less dense layer with a nanosphere texture similar to that seen in the voids below. In some places, this void even connects with the lower-layer voids. The voids in this layer are somewhat uneven in shape, but they are consistently present across the film surface. Notably, the distance from the dense stripe to the top of the low-density void is about 25 nm, which, given uncertainty about composition on top of the void, is very close to the 30 nm nanoparticle layer determined by ellipsometry. Probably this strange layer is a cross-sectional TEM view of the nanoparticles previously observed on the surface of the film with SEM. The low-density interiors then provide a potential explanation for how such large nanoparticles can form on top of such a thin film.

Also, EDS did not indicate that sodium content of the film rose above the general noise level at any point. For sodium at atomic concentrations of less than a couple percent this is possible, but we were unable to detect sodium with EELS either. Since STEM-EDS cannot accurately resolve oxygen content and did not detect any sodium, it cannot resolve the question of doping mechanism on its own. However, the STEM data is sufficient to cast doubt on sodium ion intercalation as the doping mechanism.

3.3.2 XPS Data

We also performed XPS with depth profiling on different samples in order to better answer the question of oxygen vacancy doping. XPS performs better with lighter materials like oxygen than EDS, and moreover has sufficient energy resolution to distinguish between oxidation states of metals. This means we can both quantify oxygen percent concentration throughout the depth of our film, and also detect the presence of more metallic states of indium and tin.

We first measured low-resolution broad energy spectra of the surfaces of several samples, which is a fast, non-destructive measurement. As expected, we generally observed peaks from indium, tin, and oxygen, as well as a carbon peak due to typical carbon contamination. In Figure 15, we show an example of these spectra for three samples of ITO on glass: one as-received, one reduced to about $100\,\mathrm{mC/cm^2}$, and one reduced to about $1000\,\mathrm{mC/cm^2}$. Although these three spectra have a lot in common, close inspection reveals some notable distinctions.

First, the amplitude of the tin doublet peaks appears to be suppressed as reduction increases, suggesting disproportionately low tin content at the nanoparticle surface. Second, the peak on the far left increases in amplitude and changes shape. In the non-reduced ITO, we can simply attribute this peak to contributions from indium Auger processes. However, this Auger peak significantly overlaps with the location of the sodium 1s peak. The shape change could be indicative of some sodium presence, as others have observed [61]. Unfortunately, due to the indium overlap, it is nearly impossible to quantify.

We also performed two high-resolution depth profiles focused on just the indium, tin, and oxygen peaks, plus the carbon peak for reference, for a non-reduced sample and a sample reduced for 180 s. High-resolution energy spectra were taken in between sputtering the sample for one minute with an argon ion beam. The non-reduced sample was sputtered for a total of 26 minutes and the reduced sample for 30 minutes. Alternating Zalar rotation was used to ensure an even and uniform sputter. In Figure 16 we can see how the percent composition of the each sample changed over the depth, for which sputtering time is a proxy variable.

The first point in each depth profile shows lower concentrations of indium and oxygen due to carbon contamination. After just a minute of sputtering, though, the carbon is essentially gone and we can see the true composition of the film. For the non-reduced sample, the composition is basically constant throughout the entire depth. In fact, this sample is nearly stoichiometric indium oxide with a small concentration of tin, as expected.

However, the reduced sample shows a more interesting profile. Near the surface, indium concentration is higher than in the non-reduced sample while tin and oxygen concentrations are lower. After a little bit of sputtering, tin concentration briefly increases to slightly above its value for the non-reduced sample, then gradually recovers to the expected concentration. Meanwhile, oxygen and indium steadily and linearly move back to approximately stoichiometric

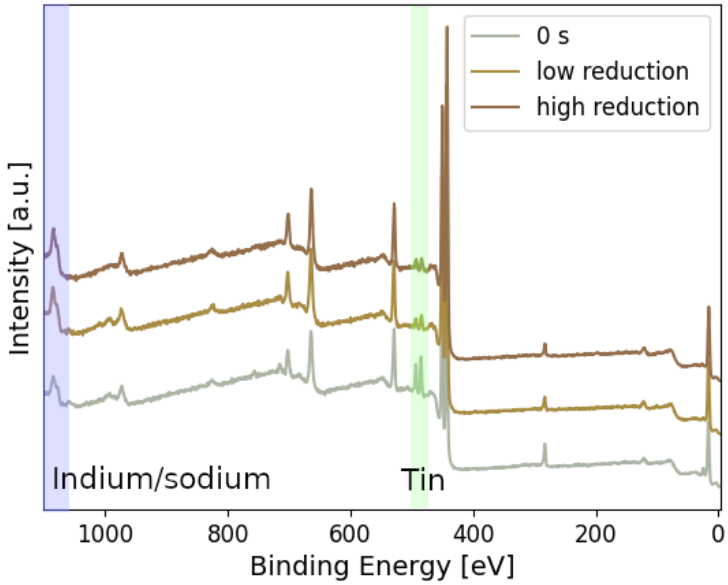

Figure 15: Low-resolution broad energy XPS spectra for three different samples of ITO on glass: one as-received, one reduced to about $100\,\mathrm{mC/cm^2}$, and one reduced to about $1000\,\mathrm{mC/cm^2}$. Units are arbitrary, but scaling is the same for all three. All three spectra are similar, but there is a notable reduction in tin doublet peak intensity (around 500 eV, highlighted in green) as reduction time increases. Additionally, the far left peak (around 1100 eV, highlighted in blue) is a very broad indium Auger peak which overlaps significantly with the location of the sodium 1s peak. As reduction increases, the peak shape does change, perhaps indicating an increasing sodium peak.

values, matching the non-reduced film after about 30 minutes of sputtering. Clearly, reduction of ITO does remove oxygen, and it does so from the surface downward.

We can also inspect in more detail the specific peak shapes at each point in the depth profile to understand, for instance, whether the indium near the surface is still partially oxidized or if it may be fully metallic. Figure 17 shows these high-resolution peak shapes for indium, tin, and oxygen of the reduced ITO sample. Peaks near the top are those measured at the surface of the film; near the bottom, deep in the bulk.

Notably, peaks associated with all three species broaden near the surface, where oxygen deficiency was observed. The indium and tin peaks broaden toward lower energy levels, associated with more metallic chemical states. Tin, in particular, clearly exhibits secondary peaks a couple of eV below the fully oxidized doublet at 485/496 eV. On the other hand, the oxygen peak broadens toward higher energy levels, also associated with bonding metals in more metallic states. All of

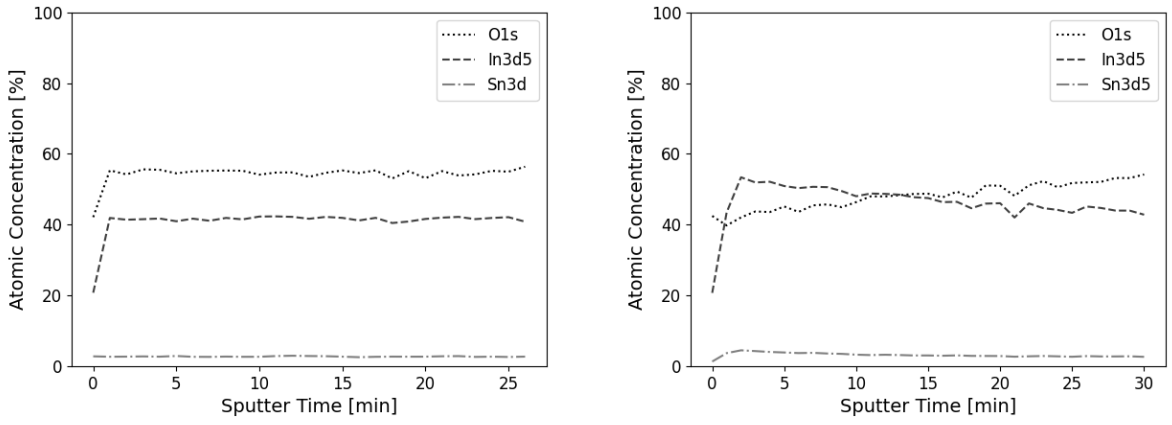

(a) (b)

Figure 16: Atomic concentration by percent measured in depth profiles for a non-reduced sample (left) and a sample reduced for 180 s (right). The first point, before any sputtering, shows low concentrations due to carbon contamination. The composition of the non-reduced sample is nearly constant over the depth, while the reduced sample shows a steady decrease in oxygen concentration toward the surface.

these features are consistent with surface-level high-resolution XPS observations made by Liu et al. [62] on ITO electrochemically reduced under various conditions.

An additional observation worth mention is that after the depth profile was complete, the reduced film which was sputtered back to near-stoichiometric ITO became almost fully transparent again, recovered from a matte-translucent reddish-brown. We also measured the transition temperature of both the sputtered and pristine film, and found superconductivity was severely degraded by sputtering. The transition temperature of the sputtered film was lower and the transition was much broader overall. In other words, mechanical removal of the oxygen-deficient layer reversed the color change and degraded superconductivity.

Electrochemical re-oxidation was reported by others [7] and reconfirmed by us to reverse color change as well. Also, as we saw earlier, annealing in air at sufficiently high temperatures can reverse the color change. Altogether, this strongly suggests that color change in ITO is mostly confined to the film surface and is likely attributed to oxygen vacancy defects.

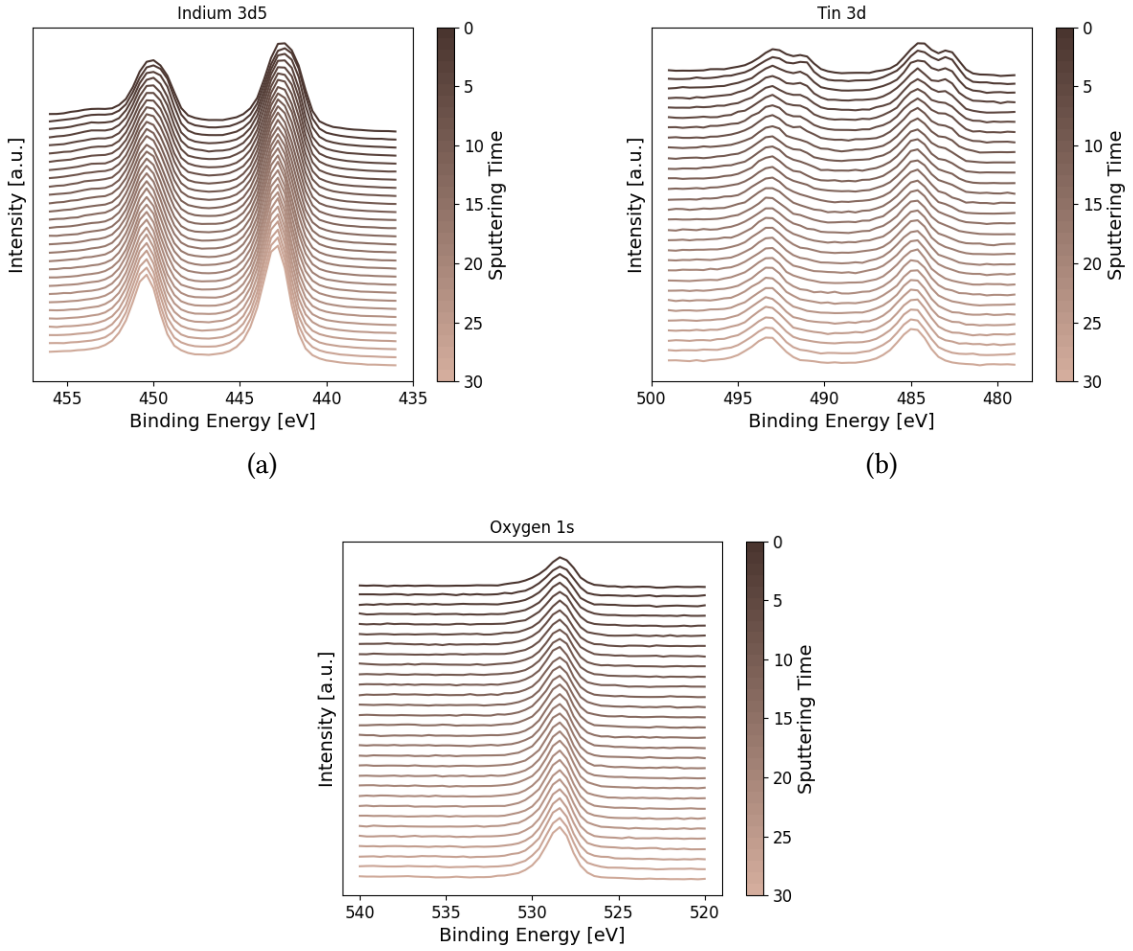

Figure 17: Evolution of peak shapes throughout the depth profile on the reduced sample. Toward the surface, the indium and tin peaks are broadened toward lower energies, indicating presence of more metallic compounds. However, the shape associated with more stoichiometric compounds deep in the film is still present at the surface as well, so the film is likely not fully metallized. The oxygen peak correspondingly broadens toward higher energies near the surface.

3.4 Implications to Film Structure of Reduced ITO

In summary, our structural and electronic analyses show that reduction causes the onset of superconductivity alongside growth of a dense nanoparticle layer on the surface of ITO. These nanoparticles exhibit different size regimes, possibly formed at different times during the reduction, and are fairly uniform up until a certain level of reduction charge density is reached. Then the nanoparticle layer becomes inhomogeneous in depth, almost lumpy in appearance, with

large nanoparticles randomly interspersed over the film surface. STEM imaging hints that these nanoparticles could be nearly hollow, but further study would be needed to confirm that.

Compositional analyses do not find conclusive evidence of sodium ion intercalation but are strongly indicative of oxygen vacancy doping. There was always some oxygen present in the depth profile, though, so the nanoparticles are likely still ITO rather than an indium-tin alloy. Additionally, it appears that the oxygen vacancy level is depth-dependent, with most oxygen removed close to the surface. Superconductivity is also apparently confined to the surface layers.

Altogether, these data strongly imply that electrochemical reduction of ITO results in growth of an oxygen-deficient layer of ITO nanoparticles, which are less transparent than the parent material but also superconducting. Although the measured transition temperatures could be compatible with patterning of electronics, it is unclear what effect the peculiar morphology of the nanoparticles may have on electronics.

4 Optical Properties of Reduced ITO

As discussed in the introduction, the best material for transparent superconductor applications is one which minimizes absorptance. Therefore a key question for the reduced nanoparticle film is whether it still has the characteristic low absorptance of ITO, and in particular whether its absorptance is lower than that of a highly reflective, highly absorptive superconductor like niobium. In order to make this determination, we must measure the optical properties of our reduced ITO film. We can measure the complex refractive index indirectly, though it will be necessary to first decide on an optical model to extract the index.

4.1 Modeling Optical Constants of ITO

According to Jung [52], ITO has a vertically inhomogeneous structure which can be difficult to analyze well with a single layer model. Additionally, its optical properties are highly dependent on factors like carrier concentration and crystallinity that may vary with deposition conditions. Authors such as Lohner et al.[51] have developed techniques attempting to account for this structural grading, but Jung's simpler three-layer method seems to be the best to date at minimizing mean squared error (MSE) between the model and the measured values of optical constants.

The simple Cauchy dispersion equation can be a good way to get a reasonable initial estimate of the optical properties of an ITO thin film, but ultimately the Drude-Lorentz oscillator model is more precise [51]. Jung uses the Drude-Lorentz oscillator model and treats the film as having three independent uniform layers: a highly disordered bottom layer about 30 nm thick, an upper layer comprising most of the remaining thickness, and a thin surface roughness layer at the very top which is half void and half ITO. Lohner et al. found that including the surface roughness layer makes the single biggest difference in the MSE.

We utilized a simplified and slightly modified version of this model based on a dispersion law programmed into the Semilab VASE ellipsometer for ITO before reduction. First we tried a single layer of ITO modeled by a Tauc-Lorentz dispersion law [67], which is commonly used for amorphous semiconductors, added to a Drude oscillator law [68]. However, we ultimately found a simple Drude-Lorentz oscillator law with two Lorentz oscillators to provide a better fit over a broader range of wavelengths. Following Jung, we also added a thin surface roughness layer on

top. We found that addition of an independent bottom layer was not necessary. We were only able to fit samples deposited on silicon, as the glass slides were too transparent and reflective for effective ellipsometry. We used the same ITO on silicon samples whose sheet resistances were reported on in Chapter 3. The post-reduction samples used for these measurements are shown in Figure 18.

Figure 18: Photograph of the ITO on silicon samples used in ellipsometry measurements. From left to right, we see a non-reduced sample, then samples reduced for 60, 90, 120, 150 and 180 s. Though the samples have already been subdivided for other experiments by this photo, the upper and lower samples represent the "a" and "b" reductions, and they were all originally the same size and shape.

For reduced ITO, based on our findings of the structure and composition, we assumed a lower layer with optical properties unchanged by reduction with some new layer on top to represent the nanoparticles. We considered different models for the nanoparticle layer. Some authors have suggested using two Lorentz oscillators to model metallic nanoparticle layers [69, 70]. Additionally, if the nanoparticles really are still ITO, we should still expect them to have a band gap and other ITO-like optical features, even if they might also now exhibit some plasmonic nanoparticle-like features [15]. We opted to model these with the non-reduced ITO Drude-Lorentz oscillator as the starting point, and allow its properties to vary.

The total stack for reduced ITO consisted of an underlying layer of unchanged ITO, with fixed optical constants but thickness as a fitting parameter; and an upper layer of ITO with tunable thickness and optical constants. Overall, this model has eleven independent parameters. Two of these parameters are the thickness of the underlying ITO and the thickness of the nanoparticle layer. Six of the remaining parameters are the location, width, and strength of the two Lorentz oscillators; two are the location and width of the Drude oscillator; and the last is ϵ_∞, the constant

contribution to the dielectric constant from higher-frequency processes.

With this model, we achieved $R^2 > 0.997$ for all the samples, although at low reduction times often $R^2 > 0.999$. Higher reduction times were generally harder to fit with any attempted models, but likely there comes a point where the nanoparticles are essentially an entirely different material than ITO. The parameter values used to fit the layer thicknesses are shown in Table 3, and the parameter values used to fit the nanoparticle optical constants are shown in Table 4.

Although we should take caution not to read too deeply into these fitting parameters, some general trends are quite clear, and strong enough to have emerged even when we explored different optical models.

Sample ID	Bulk Thickness [nm]	Nanoparticle Thickness [nm]
Non-reduced	136 - 138	-
60 s (a)	121	48
60 s (b)	120	50
90 s (a)	120	59
90 s (b)	121	69
120 s (a)	112	71
120 s (b)	120	62
150 s (a)	112	73
150 s (b)	119	77
180 s (a)	113	79
180 s (b)	117	91

Table 3: Thicknesses resulting from fitting the Drude-Lorentz model for the reduced ITO bilayer.

The clearest trend is the increase in nanoparticle layer thickness as reduction time increased. Reassuringly, this growing thickness would seem to align with earlier results from cross-sectional SEM, STEM, and AFM. Indeed, we used our ellipsometric model on an eleventh sample which we had also performed SEM and AFM measurements on, shown in Figure 19. The AFM probe saw a total depth of 77 nm from the top of the nanoparticle layer to the deepest it could reach between them. Our ellipsometric model predicted the nanoparticle layer was 85 nm thick, relatively close agreement. The AFM could plausibly underestimate thickness, if it is unable to detect the true bottom of the film between the nanoparticles, while the ellipsometric model could plausibly overestimate thickness, if it is including some of the voids observed with STEM as part of the

Sample ID	E_0^1 [eV]	f^1	Γ^1 [eV]	E_0^2 [eV]	f^2	Γ^2 [eV]	E_p [eV]	E_Γ [eV]	ϵ_∞
Non-reduced	3.75	0.16	0.62	4.30	0.44	0.24	1.10	0.23	3.50
60 s (a)	3.28	0.14	0.93	4.30	0.35	0.55	0.66	0.44	1.44
60 s (b)	3.24	0.27	1.36	4.22	0.22	0.32	0.84	0.43	1.47
90 s (a)	3.36	0.26	1.22	4.29	0.25	0.54	0.67	0.45	1.42
90 s (b)	3.14	0.30	1.42	4.19	0.18	0.43	0.74	0.44	1.53
120 s (a)	3.45	0.49	1.13	4.31	0.15	0.58	0.60	0.28	1.57
120 s (b)	3.40	0.40	1.34	4.37	0.27	0.67	0.68	0.43	1.40
150 s (a)	3.36	0.47	1.14	4.23	0.17	0.73	0.68	0.32	1.63
150 s (b)	3.21	0.36	1.41	4.25	0.21	0.63	0.70	0.40	1.44
180 s (a)	3.22	0.44	1.19	4.19	0.25	0.93	0.63	0.31	1.58
180 s (b)	2.98	0.42	1.37	4.18	0.30	0.96	0.69	0.36	1.47

Table 4: Optical constants resulting from fitting the Drude-Lorentz model for the reduced ITO bilayer.

nanoparticle layer.

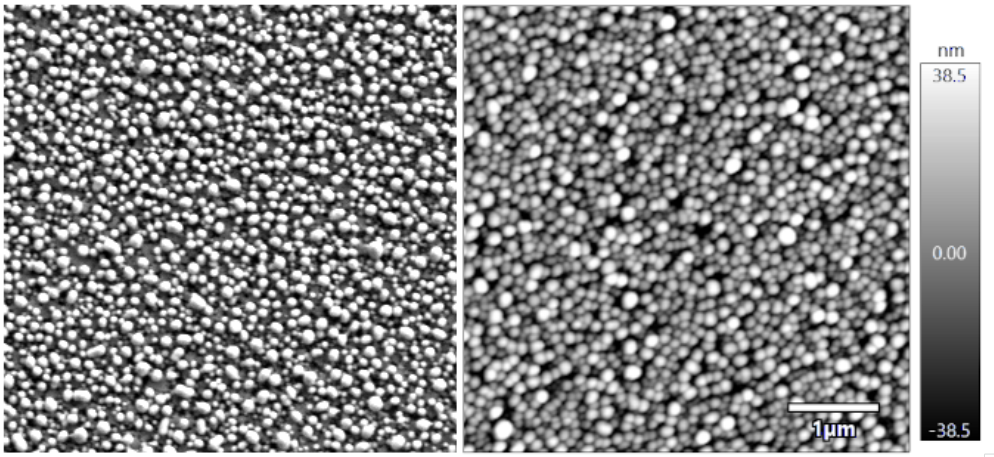

Figure 19: SEM (left) and AFM (right) images of the nanoparticle layer on a sample reduced for 120 s. The AFM found the layer to be 77 nm deep, and our ellipsometric model found it to be 85 nm thick, indicating good agreement between the different methods.

In fact, in this regime the nanoparticle layer thickness increases roughly linearly with reduction time. A linear regression of the data is shown in Figure 20. According to this model, the nanoparticle layer grew at a rate of about 0.28 ± 0.04 nm/s. However, the y-intercept of this line is 34.7 ± 5.1 nm, strongly implying a different growth regime at earlier reduction times. Additionally, although the bulk thickness does somewhat decrease as the nanoparticle thickness

increases, its decrease is insufficient to fully explain the nanoparticle growth. In fact, a linear regression barely even seems to be appropriate for describing the data, and the predicted slope of 0.05 ± 0.02 nm/s is entirely too small to indicate direct conversion of the bulk into nanoparticles.

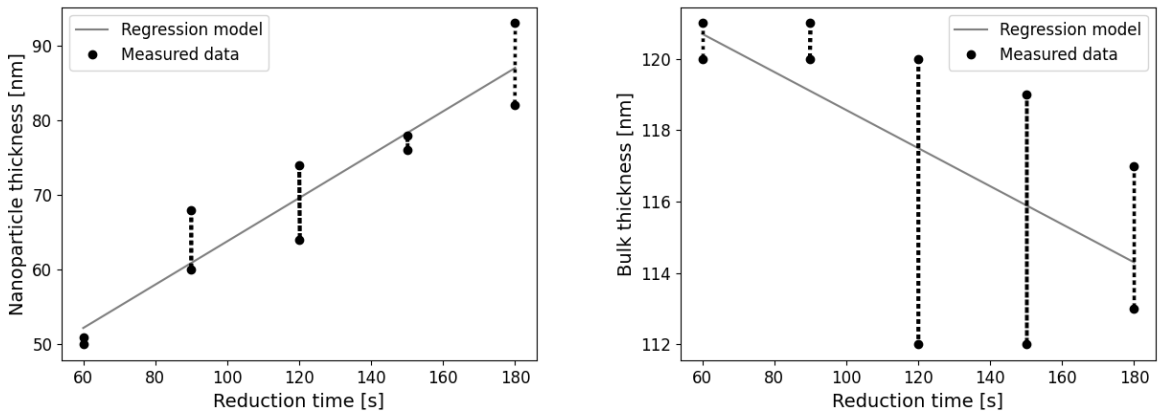

(a) (b)

Figure 20: The nanoparticle layer thickness (a) increased with reduction time with a fit line of $(0.28 \pm 0.04)[\mathrm{nm/s}]t + (34.7 \pm 5.1)[\mathrm{nm}]$. Meanwhile the bulk layer thickness (b) appears to somewhat decrease with reduction time, but the trend is less clear. The best fit line is $(0.05 \pm 0.02)[\mathrm{nm/s}]t + (123.9 \pm 2.9)[nm]$.]

Other prominent trends include an increase in the strength and decrease in energy of the lower-energy Lorentz oscillator around 3 - 3.75 eV; and broadening of the higher-energy Lorentz oscillator around 4.2 - 4.3 eV. The Drude plasma frequency and the core permittivity appear to suddenly decrease with any reduction and then remain fairly constant with increased reduction time. Other trends seem to appear or disappear depending on whether the non-reduced ITO is included as a "zero-second reduction" point or not, and are probably unreliable.

The changes to the lower-energy Lorentz oscillator, in particular, would appear to explain the observed optical changes to ITO. As it becomes stronger and moves to lower energies, it can induce more absorption of blue light in the material. With more blue light absorbed, the light reflected off the film is redder, as we observed. Another way to think of this absorption is that it occurs below the band gap energy of ITO, effectively shrinking the band gap. The higher-energy Lorentz oscillator simply broadens, which could be associated with general increase in electron interactions with defects introduced by the reduction process.

Meanwhile, it may seem counterintuitive that increasing the carrier concentration by intro-

ducing oxygen vacancies could decrease the Drude oscillator frequency, since we saw earlier that typically carrier concentration and plasma frequency are directly proportional, and the Drude frequency typically corresponds to the plasma frequency in this model. However, when deriving this relationship we assumed a homogeneous bulk material. The electronic behaviors of conductive nanostructures are set in part by their bulk material properties, but also in part by their specific geometry. We may not be observing the true plasma frequency but rather the frequency of the surface plasmon resonance (SPR), which for spherical nanoparticles is related to the plasma frequency in equation 40, with ϵ_m the permittivity of the medium in which the nanoparticles are embedded [15]. Note that in this terminology, the "surface" of the material is anything less than the metallic skin depth away from the air-metal interface. The skin depth is inversely proportional to the absoprtion coefficient, and based on our refractive index calculations for ITO this will be on the order of a micron for the wavelengths measured by ellipsometry. Effectively, then, the entire nanoparticle layer is "surface." In the equation:

$$\omega_{SPR}^2 = \frac{\omega_p^2}{\epsilon_\infty + 2\epsilon_m}, \tag{40}$$

since the denominator is always greater than one, we can see that this plasmonic resonance effect will always decrease the energy of the apparent Drude frequency. If we assume the nanoparticles have the same fundamental plasma energy as the underlying ITO – likely an underestimate – and the predicted high-frequency dielectric constant of about 1.44, embedded in air, this formula suggests a Drude oscillator at around 0.6 eV, consistent with our ellipsometric model. The slightly higher oscillator energies observed in the model are likely a result of the increased carrier concentration and a higher fundamental plasma frequency compared to our estimate.

With some understanding of the underlying physics in the changes to the optical constants with reduction time, we can look at the refractive index and extinction coefficient extracted from this model. Figure 21 shows the computed optical constants for the models outlined above. Notably, the real part of the refractive index shifts down upon reduction, mostly due to the large decrease in the high-frequency permittivity. The extinction coefficient generally increases with reduction, although it depends a little on the wavelength range. In blue wavelengths, the growing Lorentz oscillator leads to a signficantly increased extinction coefficient. However, the plasmonic

redshift of the Drude oscillator seems to actually decrease the extinction coefficient for some redder wavelengths.

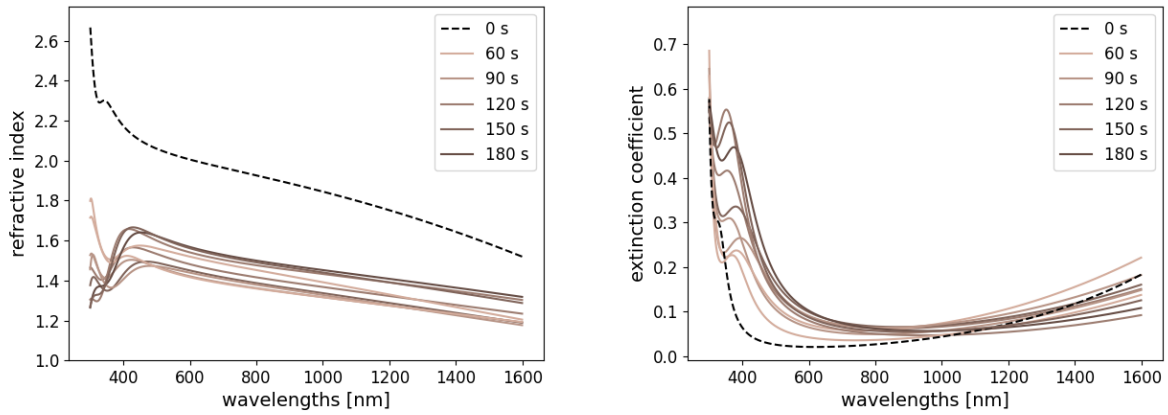

(a) (b)

Figure 21: Refractive index (a) and extinction coefficient (b) for ITO reduced for different lengths of time. Reduction generally decreases the real part of the refractive index of the film while increasing the extinction coefficient.

The ellipsometric model produces reasonable predictions that agree well with observed behaviors such as nanoparticle growth and increased blue-light absorption with reduction time. The optical constants extracted from this model are likely reliable enough to use in comparisons of absorption in reduced ITO versus other materials in order to evaluate its usefulness in transparent superconductor applications.

4.2 Absorption in Reduced ITO

From the refractive index and extinction coefficient of reduced ITO extracted by ellipsometry, we can use the Fresnel equations to compute the reflectance, transmittance, and absorptance of different thicknesses of our film and different angles of incidence. We will consider the reflection off the vacuum-to-conductor interface, and then absorption occurring over passage through a finite thickness of film, but we will ignore secondary reflections for this analysis. Since we determined that superconductivity may be confined to the nanoparticle thin film, we will simplify our analysis by only considering absorption in this layer. For purposes of comparison, we will also compute the reflectance, transmittance, and absorptance of niobium, a commonly used material

in superconducting electronics that has a high refractive index and extinction coefficient in the optical regime. This comparison will help us understand under which conditions ITO can provide an advantage over standard materials by decreasing absorption and, by extension, quasiparticle formation and associated deleterious effects.

In Figure 22, we show the percentage of light transmitted, absorbed, or reflected from normal incidence from air onto a 100 nm thick film of nanoparticles or non-reduced ITO. We note that the values for non-reduced ITO, calculated from our refractive index model, agree well with directly measured values of 100 nm thick sputtered ITO reported in the literature [71]. We can see that reflection is generally low for ITO, but higher for the non-reduced ITO than the nanoparticles. For bluer wavelengths, the non-reduced ITO is less absorptive than the nanoparticles, while for redder wavelengths it is more absorptive.

Generally the fundamental optical properties of the films reduced by different amounts are actually rather similar when keeping thickness constant; changes to the refractive index are not quite sufficient to explain the observed color change. Consider what light causes the color though: because the films are not very reflective, a lot of the color actually comes from secondary reflections from the interface with silicon. As a result, the primary determinant of color will be absorption in the film. The longer light travels through the film, the more blue light is absorbed. Consider, in Figure 23, absorption computed with the appropriate nanoparticle layer thicknesses as well. When we use the actual measured thicknesses in our calculation, we see that absorption in the samples with lower reduction times is considerably reduced, from about 60% to about 40% absorption in the Lorentzian peak.

As we have seen, increasing the thickness of the film causes more absorption, without changing the reflection. However, we have another major variable that affects the optical behavior: angle of incidence. As the angle of incidence becomes more oblique, more light is reflected, which decreases the amount of light available to be absorbed. On the other hand, the light travels longer within the film, which increases the fraction that is absorbed rather than transmitted. Competition between these effects depends on the refractive index.

In Figure 24, we can see that for bluer wavelengths, the more-reflective, non-reduced ITO exhibits lower absorption from light incident at a $\pi/3$ angle than from normal incidence. On the other hand, the less-reflective nanoparticle layers absorb more light, because the reflections are

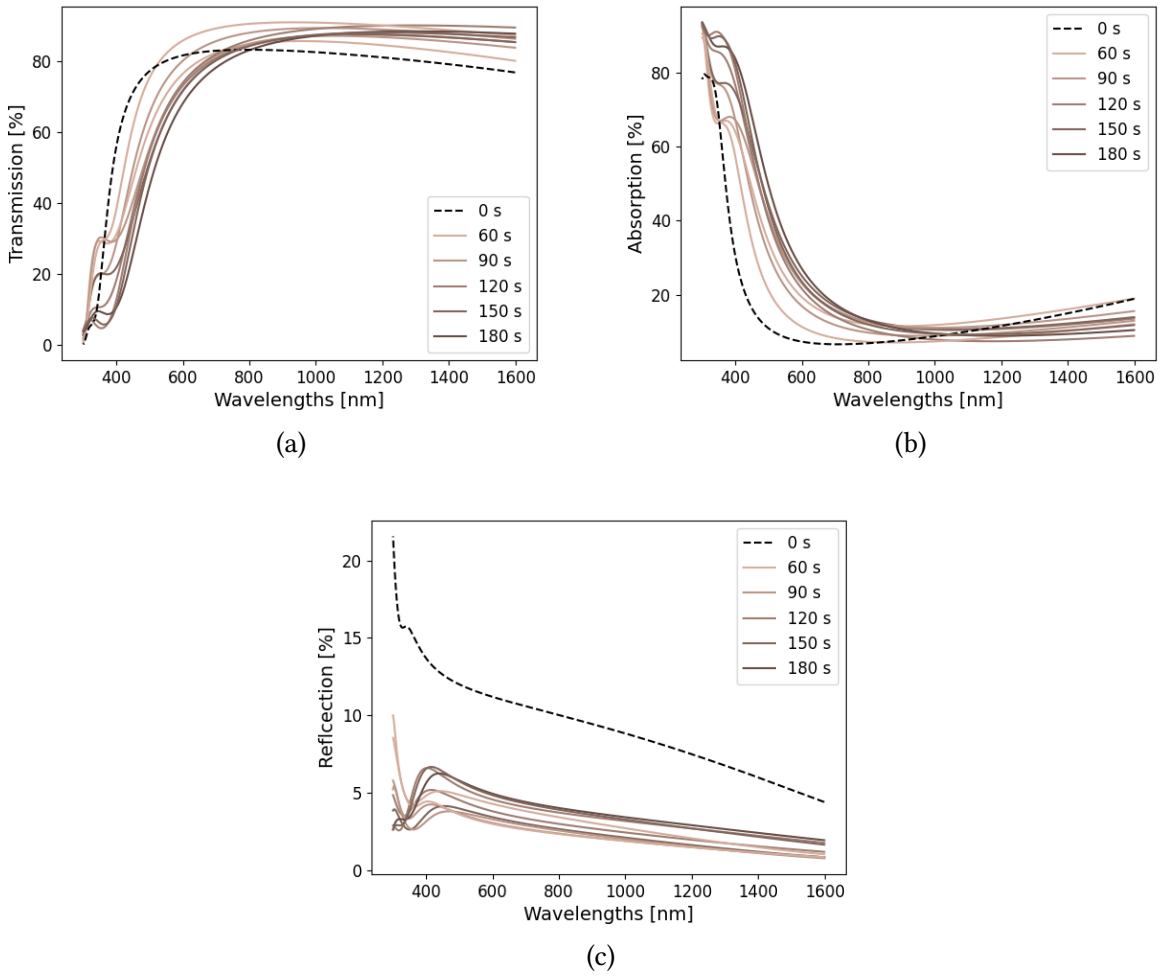

Figure 22: The percentage of light transmitted (a), absorbed (b), or reflected (c) by a 100 nm thick layer of ITO or reduced ITO for the optical constants measured with ellipsometry, assuming normal incidence

still too low to combat the increased distance traveling through absorptive material.

Now that we have some understanding of the optical properties of ITO and the reduced-ITO nanoparticles, we can compare these films to a material more commonly used in superconducting electronics, niobium. We compute the absorption of niobium from refractive index values determined by Leksina et al.[72] and compare it to absorption in ITO nanoparticles reduced for 180 s under different conditions. In Figure 25, we show absorption in niobium and ITO nanoparticles at normal or $\pi/3$ incidence and for films 10, 100, or 1000 nm thick.

Notice that the ITO nanoparticles are almost always less absorptive than the niobium, with the exception of wavelengths less than 450 nm where the Lorentz oscillator behavior dominates

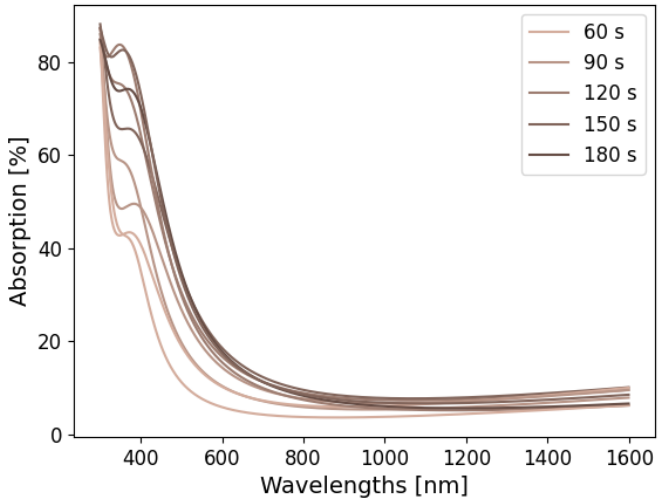

Figure 23: Absorption for nanoparticle films calculated from the appropriate refractive index model and film thickness for different reduction times. Because the nanoparticle layer is very thin at low reduction times, absorption remains very low.

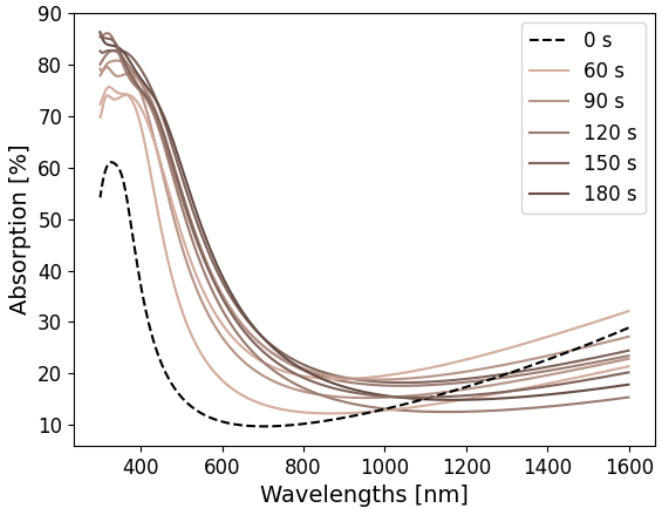

Figure 24: Absorption for 100 nm thick ITO and nanoparticle films assuming a $\pi/3$ angle of incidence. Total absorption in the ITO film is decreased from normal incidence due to high reflections, but total absorption in the nanoparticle films is increased.

and adds lots of absorption to the nanoparticles. For thin films, the benefit of ITO is especially pronounced. An ITO nanoparticle film 10 nm thick should barely absorb light above 600 nm, but a niobium film of the same thickness absorbs 40-50% of light at the same wavelengths. However, for thick films, eventually all light that is not reflected is absorbed. Since niobium is very reflective,

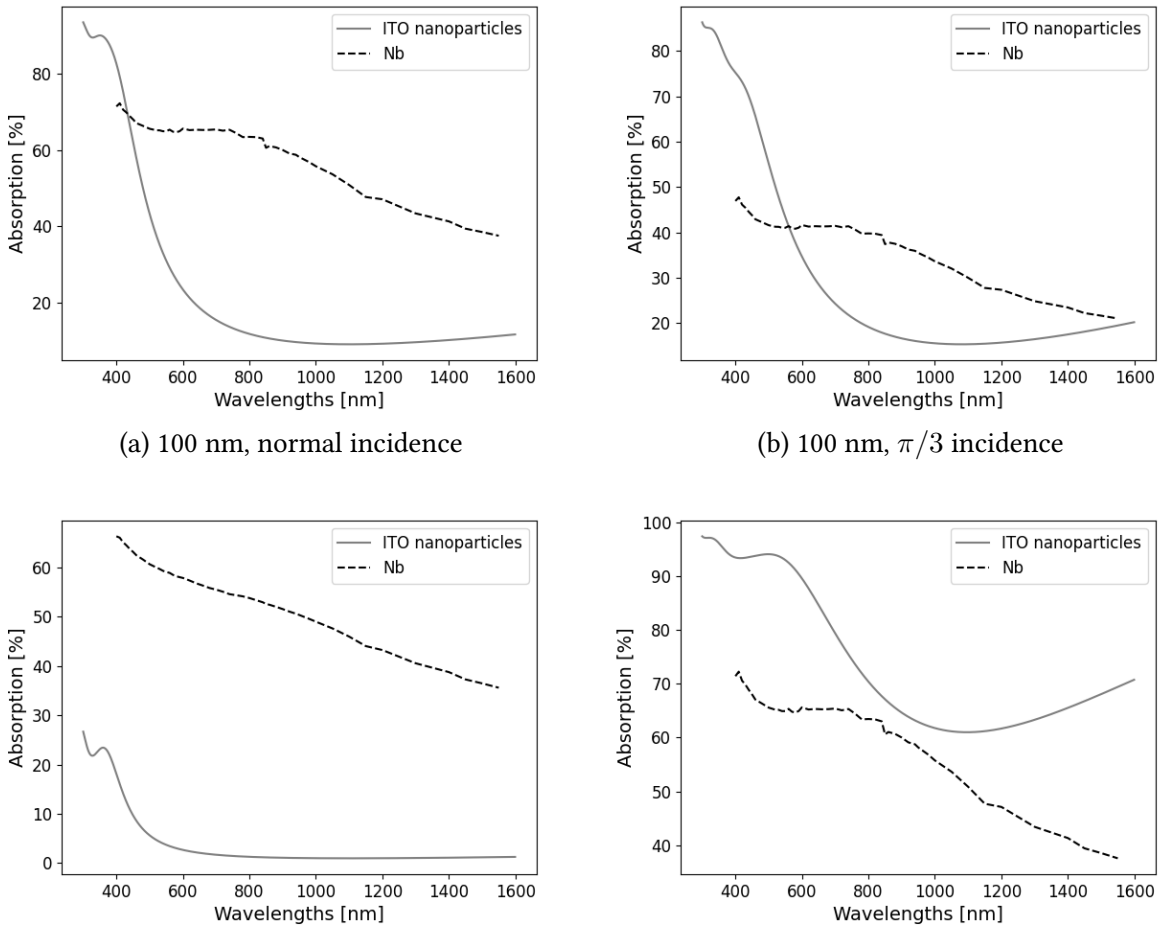

(a) 100 nm, normal incidence

(b) 100 nm, $\pi/3$ incidence

(c) 10 nm, normal incidence

(d) 1000 nm, normal incidence

Figure 25: Absorption in niobium or ITO nanoparticles reduced for 180s, for 100 nm thick film and normal incidence (a) or $\pi/3$ incidence (b), or normal incidence and 10 nm thick film (c) or 1000 nm thick film (d). Niobium is only less absorptive than ITO nanoparticles for short wavelengths or thick films. Niobium refractive indices from Leksina et al.[72]

absorption actually saturates to a lower value than in reduced ITO. For example, for a 1000 nm thick film, niobium is the less absorptive choice.

4.3 Discussion

Our optical model for the nanoparticles implies a number of rich behaviors which we have only just begun to explore. Compared to the parent material, reduced ITO has a stronger, more redshifted Lorentzian resonance near the typical band gap energy and a redshifted Drude resonance,

probably due to plasmonic resonance. Although absorption is generally increased in reduced ITO nanoparticles, particularly in blue wavelengths, it remains less absorptive than niobium under a variety of conditions, particularly for thin films. However, for thicker films or more oblique angles of incidence, the relative advantage of reduced ITO is decreased or even reversed by its low reflectance.

5 Device Fabrication and Testing

Ultimately, the utility of reduced ITO as a transparent superconductor is determined not only by its sheet material properties but also its potential for fabrication of electronics. Particularly given the unusual nature of the nanoparticle thin film structure, it cannot be taken for granted that reduced ITO is suitable for electronics. Geometric effects in inhomogeneous amorphous materials and especially nanoparticles can have either enhancing[73, 74, 75] or suppressing[37, 76] effects on superconductivity. Though generally narrower geometries and smaller nanowires increase the transition temperature, there is a possibility that the nanoparticles are only loosely connected and too thin a wire may not have a continuous superconducting path from one side to the other.

We attempted patterning of ITO by two different methods, direct patterning of the reduction and ion mill etching. We compared these methods from a practical standpoint based on the resolution and accuracy of the geometries produced, and then prepared experiments to compare the electrical quality of nanowires produced by each method.

5.1 Direct Patterning of Reduction

An intriguing option for patterning reduced ITO which is not possible for other superconducting materials is direct patterning of the reduction. This option is appealing in its simplicity. Since reduction only appears to occur in areas directly exposed to current, it can be blocked on specific regions by a mask of insulating photoresist. Then in principle the patterning and development of the resist is the only extra step; no etching is required, since the non-reduced ITO is not a superconductor.

5.1.1 Methodology

In order to directly pattern the reduction, we spun on a layer of S1813 photoresist and baked it for 90 s at 100 °C. This resist was exposed in a Heidelberg μPG 101 at 8 mW with 25% duty cycle, and developed in CD26 for 60 s. The resulting sample was reduced in our three-electrode electrochemical cell, with current and time adjusted to maintain proper reduction charge density for the smaller exposed area. After reduction, the remaining photoresist can be cleaned off with

acetone and IPA. Samples were then attached with thermal varnish and wirebonded to a PCB for testing.

5.1.2 Resolution of Directly Patterned Wires

At first glance, the process appears to work quite well. Direct patterning produces sharply delineated wires with widths within $\pm 0.2\,\mu\mathrm{m}$ of the designed widths, as seen in Figure 26. Some messy-looking residues off the sides of the wires are most probably photoresist that was not sufficiently removed by a simple acetone and IPA rinse prior to annealing; the procedure was later changed to include a sonication cleaning step before annealing in order to more thoroughly remove photoresist.

However, while the successful wires appear well-fabricated, other wires patterned by the same intercalation failed to connect and were broken off in the middle. Thin wires were more vulnerable to this failure mode than thick wires. While this could indicate insufficient development of the photoresist, it may also point to more fundamental current dynamics at play. For unknown reasons, none of these first wires exhibited any nonlinearity in the current-voltage curve that would indicate superconductivity.

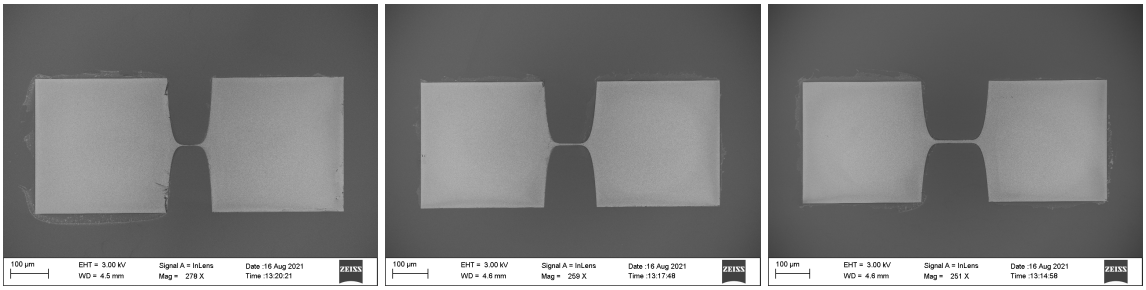

(a) 2 µm wide wire (b) 5 µm wide wire (c) 10 µm wide wire

Figure 26: SEM images of microwires directly patterned from reduction to about 75 mC/cm^2, all on the same chip. Measured widths are all within $\pm 0.2\,\mu\mathrm{m}$ of design values. The residue at the edges is photoresist that was not sufficiently cleaned off prior to annealing; later trials involved full sonication prior to any annealing steps.

5.1.3 Wider Wires

We made a second attempt, this time with much wider wires of 100, 125, 250, 500, 1000, and 2000 $\mu\mathrm{m}$, also reduced to about 75 mC/cm^2. We planned to do 4-point transition temperature measure-

ments on each wire in addition to current-voltage measurements to help debug any issues. We also evaporated gold-titanium pads on top of the wider wires in order to facilitate wirebonding, which we found to be difficult on reduced ITO probably due to its low carrier concentration and strange morphology. The method for patterning the wires was the same as before, but with a second patterning process for the contact pads. To pattern the contact pads, we spun PMGI SF8 at 4500 RPM for 60 s, then baked for 90 s at 180°C. Then we also spun a layer of S1813 at 4500 RPM for 60 s and baked for 90 s at 100°C. We exposed this resist in the Heidelberg at 7 mW with a 20% duty cycle, and developed in CD26 for 80 s. Finally we evaporated 10 nm of titanium and 50 nm of gold on top. Especially for films at low reduction charge densities, we found the metallic contact pads were quite helpful for wirebonding.

These wires were large enough to be clearly visible under an ordinary optical microscope. Photographs of these devices are shown in Figure 27. As with the previous devices, the overall shapes of the wires are faithfully transferred by the direct patterning of the reduction, but odd effects from current dynamics are once again observed. The four widest wires appear solid, but the two narrowest wires are only faint outlines, having apparently failed to capture much reduction current. A close-up of the widest wire shows mostly uniform, expected coloration, but two of the corners appear not to have been fully reduced.

A closer look at these wires under SEM showed further insights into the effects of current dynamics during direct patterning. As seen in Figure 28, the nanoparticles at the interior of the film are smaller than expected for this reduction level, while the nanoparticles at the corner are larger. Some of these corner nanoparticles even have shapes reminiscent of bursting bubbles. It appears that some form of current crowding pulls excess current to the edges and particularly the corners of the directly patterned wires, so this technique may not be ideal for long, thin geometries with sharp corners.

As a side note, these images also provide striking insight into the boundary between the pristine ITO and the reduced ITO. The ITO that was protected by resist has a typical morphology for sputtered polycrystalline ITO, with a surface defined by small clusters of even smaller columns. Near the edge of the wire, the clusters dissolve into a more amorphous sea of very loosely-grouped columns, with increasingly large gaps in between. The gaps become larger closer to the wire edge. Inside the wire, nanoparticles seem to form on top of the remnants of the loose columnar struc-

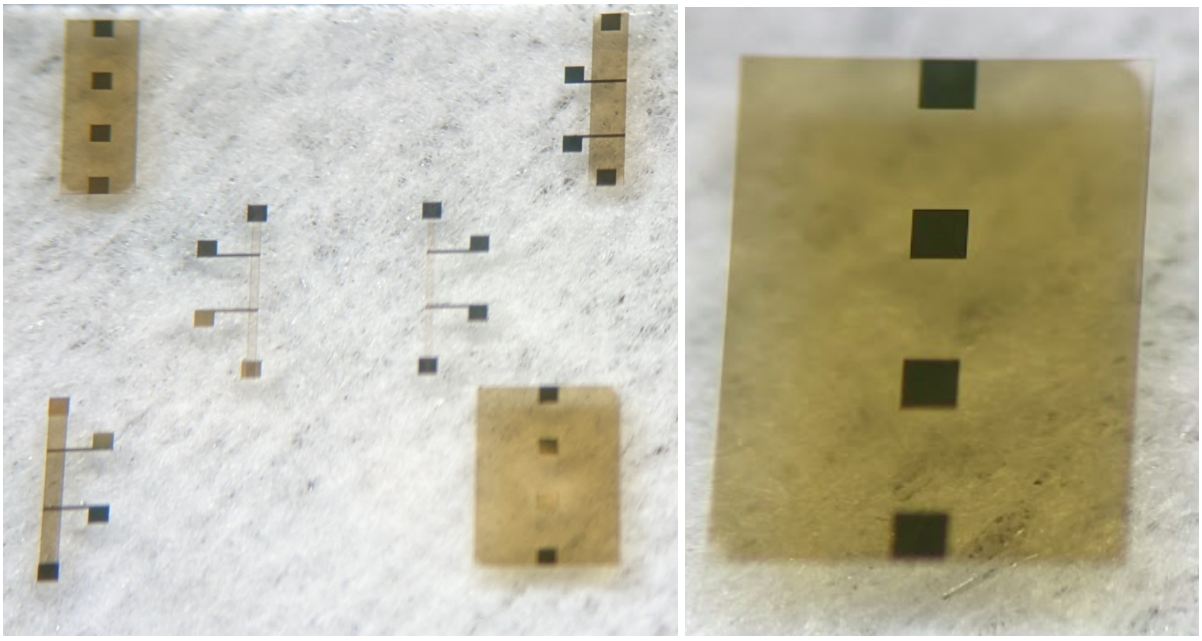

(a) (b)

Figure 27: (Left) Six wires of widths 100, 145, 250, 500, 1000, and 2000 μm that were simultaneously directly patterned, with titanium-gold contact pads for easier wire-bonding. While the four widest wires appear fine at this magnification, the two narrowest wires are only faint outlines. (Right) A closer look at the widest wire confirms its general integrity, although two of its corners appear oddly rounded off.

ture. It is interesting that, aside from the large current-crowding nanoparticles, the transition from pristine to reduced ITO is fairly smooth. We have not yet characterized these devices, but will report electrical data in future work.

5.2 Ion Mill Etching

An alternative to direct patterning of the reduction is patterning a dry etch of the material. This technique is more commonly used to pattern electronics, and is less dependent on potentially complex current dynamics. However, unlike niobium nitride and other common superconductors, ITO is not very susceptible to reactive ion etching. Our attempts to remove material with a CF_4 etch resulted in no detectable change to the thickness of the ITO, as measured by ellipsometry. This result was not too surprising since oxides are typically not very reactive. Instead, we turned to ion mill etching, which is more effective on oxides since it is a mechanical rather than a chemical dry etch.

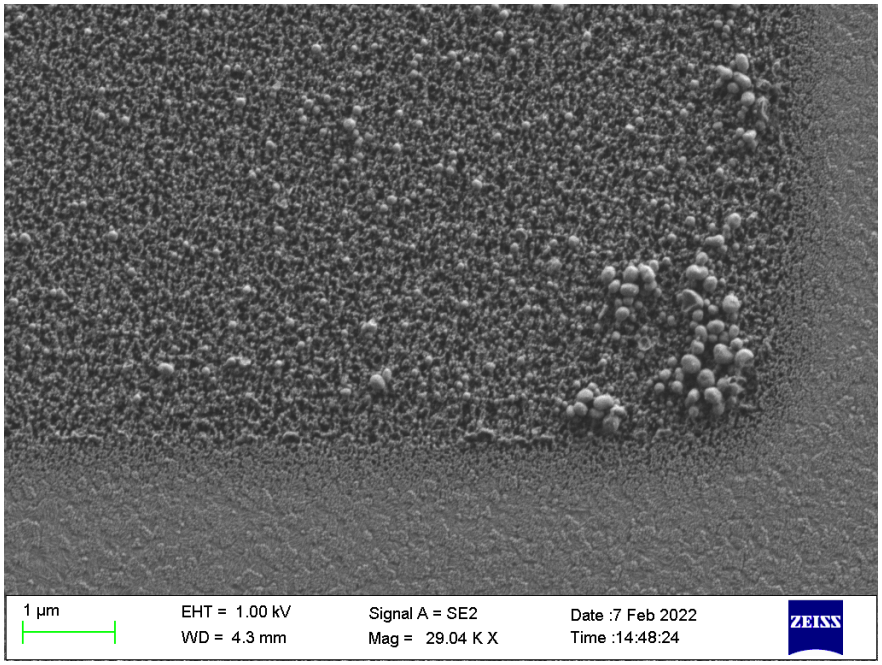

Figure 28: SEM of the corner of a directly patterned microwire $100\,\mu\mathrm{m}$ wide reduced to about $75\,\mathrm{mC/cm^2}$. Note the formation of larger nanoparticles on the edges and especially the corner, indicating some form of current crowding.

5.2.1 Methodology

We determined the etch rate of ITO and of our resist, S1813, by ellipsometric measurement of the thickness of ITO samples on silicon with and without S1813 spun on, and before and after 10 minutes of ion mill etching. We found that the ITO had an etch rate of about 10 nm/min and the S1813 about 7 nm/min. Although the resist does not etch much more slowly than ITO, we found the typical thickness of S1813 with our usual spinning method is over 1000 nm, so it should still be sufficiently protective.

Although 10 minutes of etching does not completely remove the ITO layer, it goes deep enough that it should remove all of the nanoparticles and beyond, thus creating a full gap with no superconducting material. We did not want to etch too much longer, because mechanical heating from the milling can burn resist and make it nearly impossible to remove.

To prepare the patterns for the wires, we first electrochemically reduced the film to the desired amount, then used the same process as when preparing direct patterning of the reduction. The only other difference is in the pattern itself: where for direct patterning of the reduction, we needed to expose parts of the film that we wanted to dope, for ion mill etching we exposed just

the outline of the wires to be etched away to form a gap.

Once the resist was developed, we ion milled the sample for 10 minutes at a 45° angle. Then we cleaned off the remaining resist.

5.2.2 Appearance of Ion Milled Wires

We ion milled a set of wires to match the wider directly-patterned wires, at 100, 125, 250, 500, 1000, and 200 μm. We found that milling the wires resulted in smooth gaps at very good agreement with designed values, as seen in Figure 29.

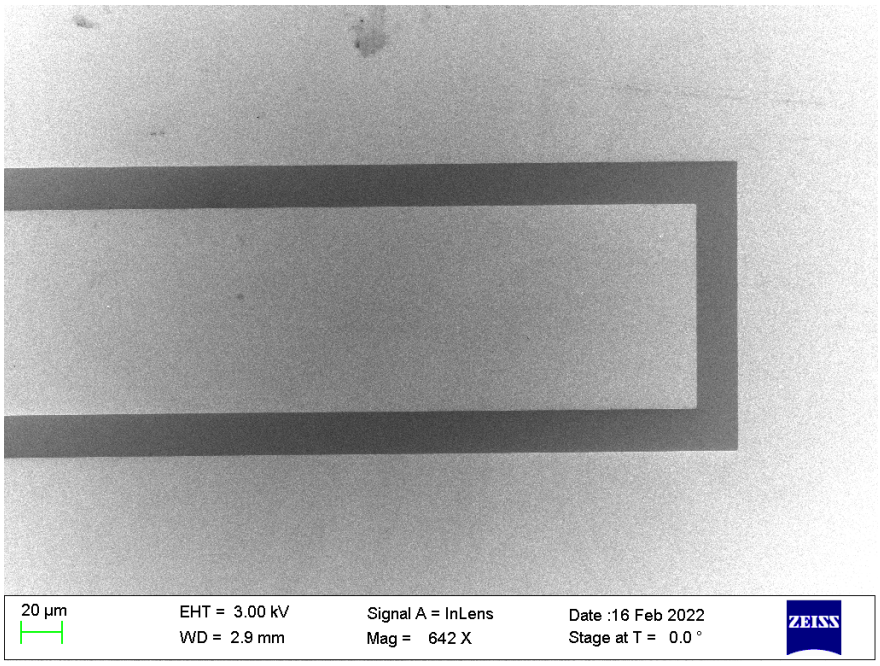

Figure 29: SEM of the end of an ion milled microwire designed for a 20 μm gap and a 100 μm width. The resulting pattern agrees well with the designed values.

The corners produced by ion milling were somewhat rounded with a radius on the order of 100 nm, as shown in Figure 30. This is not necessarily a limitation for production of superconducting microelectronics, as sharp corners are typically avoided in real designs, but seemed worth noting. Also in this figure we can make out the texture at the bottom of the milled-out gap. The nanoparticles are completely milled away as expected. What remains is a roughened surface of what should be a non-reduced, non-superconducting thin film of ITO.

Altogether, ion milling appears to be a promising technique for patterning reduced ITO electronics, resulting in relatively smooth microwires and a deep gap. The roughness of the nanopar-

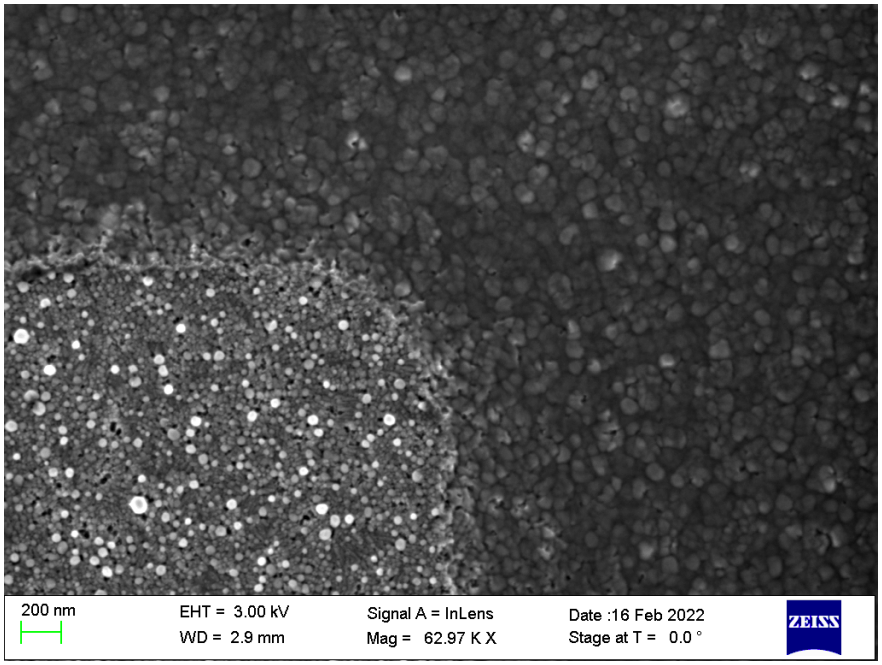

Figure 30: SEM close-up of a corner of an ion milled microwire. The corner is somewhat rounded with about a 100 nm radius and the bottom of the gap is milled well below the nanoparticles.

ticles themselves remains the most unusual geometry of the system.

We were not able to complete testing of ion milled wires within the necessary time frame, but results will be included in future work.

6 Discussion and Conclusion

Finding a transparent superconductor that is suitable for fabricating electronics would be a major step toward the integration of superconducting circuits such as quantum computers or superconducting classical readout with optical communication or detector architectures. Although a number of candidate materials have been previously discovered, their transparency was not well-quantified and no electronics made from these materials had been studied. In our work we chose one such material, reduced ITO, and thoroughly characterized its thin film properties and its potential for fabricating nanowires.

Reduced ITO is an unusual superconducting material. By simply driving a reduction current through non-superconducting ITO films, a semi-transparent superconducting thin film of oxygen-deficient ITO nanoparticles forms on top. We cannot rule out simultaneous sodium ion intercalation with our experiments, but we found that oxygen removal is by far the most significant compositional effect of reduction. XPS cannot adequately resolve sodium from indium, and STEM-EDS could not detect sodium above noise levels. However, XPS strongly indicated oxygen removal, so after long reduction times we should expect the nanoparticles to become pure indium-tin alloy. At low levels of reduction, the nanoparticles are very small, less than 10 nm in diameter, pale reddish-brown in color, and dispersed into a sparse film. As reduction levels increase, the nanoparticles become larger, denser, and more metallic in color and reflection.

These oxygen-deficient nanoparticles have a number of potentially favorable properties. The nanoparticles exhibit a tunable, dome-shaped dependence of transition temperature on carrier concentration with a transition temperature up to 4 K, consistent with other superconducting semiconductors. When reduced near the maximum transition temperature, the nanoparticles still have lower absorption than niobium in thin film conditions for red-to-near-infrared wavelengths, and show indications of surface plasmon resonance. The nanoparticle layer appears to be a fairly typical doped superconducting semiconductor, but with confirmed low absorption.

However, the reduced ITO system is also quite complicated. Superconductivity appears confined to the nanoparticle layer, the exact properties of which can change drastically depending on the properties of the parent material and on the reduction conditions in ways that are not fully understood. The nanoparticles may not be fully electrically connected, especially at low reduction

levels were they are smaller and sparser. Moreover, analysis of STEM images, combined with the knowledge that the underlying ITO layer thickness is not greatly diminished by the creation of nanoparticles, indicates the nanoparticles may be mostly hollow. The effects of these properties on potential electronics is unknown.

Our work on reduced ITO strongly indicates that superconductivity and low absorption are not mutually exclusive, and our efforts to pattern electronics from reduced ITO suggest that engineering with transparent superconductors may be feasible. However, reduced ITO nanoparticles are a challenging platform for electronics due to their rough geometry and their reproducibility difficulties. Further efforts to make electronics out of reduced ITO could include attempting to sinter the nanoparticles together to smooth them out or controlling the entire process starting with ITO deposition in order to eliminate unpredictable variables. However, if one had control over the entire process, it makes more sense to try to deposit the ITO in an oxygen-deficient form to begin with, and perhaps eliminate the rough nanoparticle geometry entirely. Nonetheless, although reduced ITO is likely unsuitable for typical superconducting electronics, it has a number of interesting properties that may find application elsewhere, as an infrared-plasmonic superconducting nanoparticle platform.

Moreover, other materials could be studied for their potential as transparent superconductors. $LiTi_2O_4$ is an especially promising candidate since it superconducts in its stoichiometric form: no post-processing should be necessary, so low surface roughness and reproducibility should be easier to achieve. The optical analysis methods we developed will be useful for evaluating and comparing new transparent superconductor candidates like $LiTi_2O_4$, and the ion milling method for patterning ITO electronics should also be suitable for other transparent conductive oxides. Although reduced ITO may not be the best platform for transparent superconducting electronics, we now have a much better understanding of its behavior as well as a combination of techniques that will aid in studies of other materials.

7 Appendix A: Electrochemical Apparatus

Although the electrochemical cell itself is a key component of reduction experiments, many papers are sparse on construction details of their apparatus. In informal early experiments we observed that rate of color change in ITO was affected by many variables: orientation of and distance between electrodes, total electrode area submerged, and even the instrumentation used for control and readout. To improve reproducibility we devised an apparatus to hold the electrodes in a consistent placement and orientation over many experiments.

The apparatus was made with simple machining techniques out of teflon, although any insulating, machinable material should be suitable for similar apparatus. It consisted of three separable components: two sample holders and one "beaker lid" to rest on the top of the beaker and fix the sample holders in place.

Each sample holder was shaped from a single cylinder of teflon with four major cuts: one to size down the shaft that would go below the lid, one to further size down the part of the shaft that rested within the lid, one to cut out the section for the sample to rest in, and one to better shape this section so that a 2 cm x 1 cm piece of ITO would always be held in the same way. The resulting shape is shown in Figure 31. One additional shaping cut allowed the sample holder to lock in place in a specific orientation, guaranteeing the samples would always face each other. Finally, a through hole down the top allowed the sample holder to be screwed into the lid so it would not move; a hole down the top and out the front allowed for wiring through the holder; and a hole in the front of the sample rest allowed for a metallic clip to be screwed in for holding the sample in place.

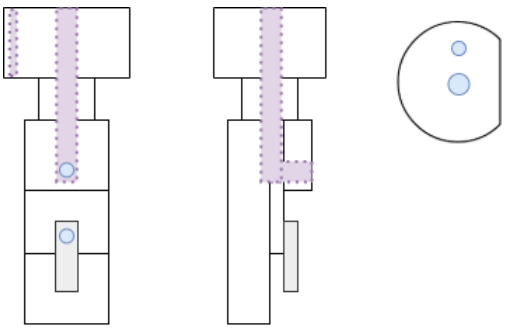

Figure 31: Front, side, and top views of the sample holder component. Purple dashed lines indicate through holes. A metal clip in the front allowed samples to be held firmly in place.

The lid consisted of a square piece of teflon, large enough to rest on the beaker below. It had three large holes through it, two symmetrical holes for the sample holders and a smaller hole for the counter electrode, which was a simple platinum wire with a larger insulating piece on top, to slip through. Two additional holes allowed for the sample holders to be screwed into place. A top view of the beaker lid component is shown in Figure 32.

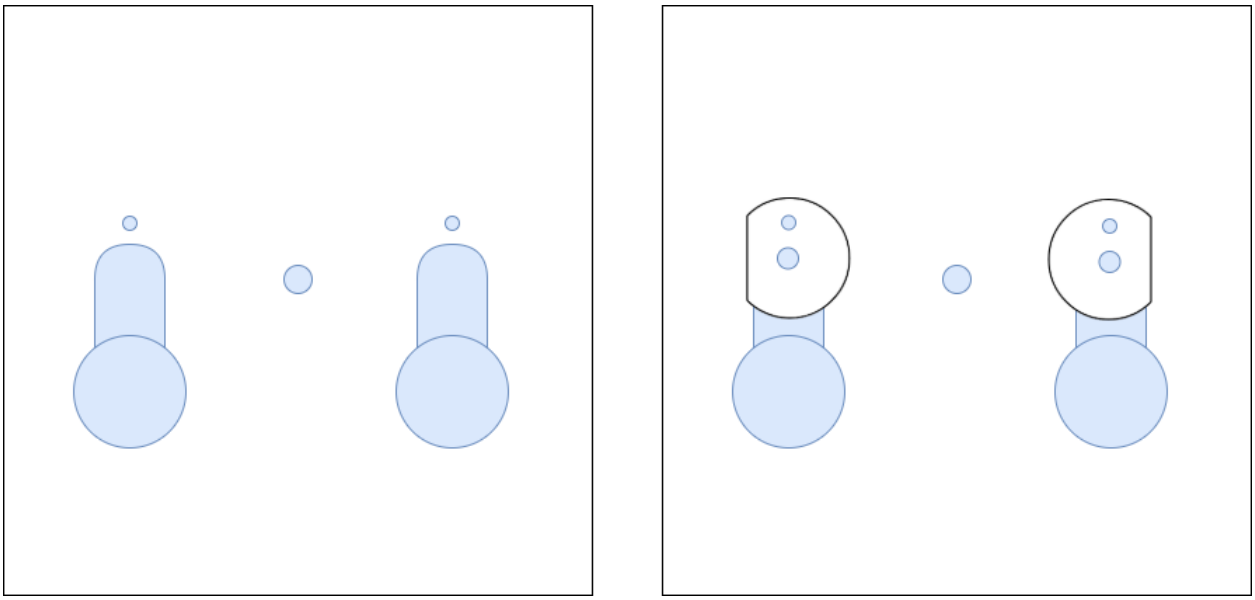

Figure 32

For operation of the electrochemical cell, the two sample holders were inserted through the lid and wires were routed down the top and out the front to connect to the metal clip. Side views of the apparatus, fully assembled with and without wiring and samples, are shown in Figure 33.

With this apparatus, we were able to perform many quick, reproducible, and uniform electrochemical reductions of ITO. In some sense this is rather informal electrochemistry, especially because the reference electrode is not fully isolated from the currents in the working cell. However, it was sufficient for our purposes.

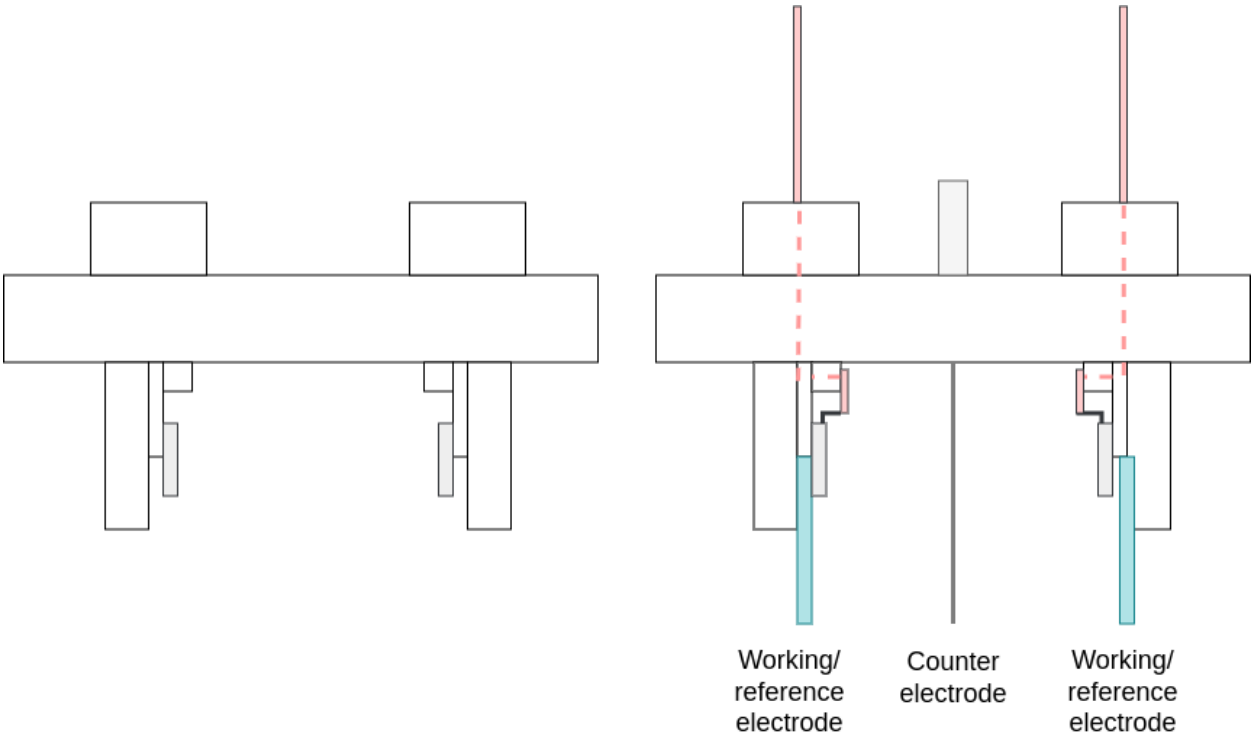

Figure 33: Side view of the electrochemical apparatus (not to scale). (Left) The assembled apparatus without any of the experimental components. (Right) The assembled apparatus with wiring and electrodes in place. Due to the symmetry of the apparatus, the working and reference electrode are interchangeable and determined by electronic setup.

References

[1] R. P. Budoyo et al. “Effects of nonequilibrium quasiparticles in a thin-film superconducting microwave resonator under optical illumination”. In: *Phys. Rev. B* 93.2 (Jan. 2016). Publisher: American Physical Society, p. 024514. DOI: 10.1103/PhysRevB.93.024514. URL: https://link.aps.org/doi/10.1103/PhysRevB.93.024514 (visited on 02/25/2022).

[2] Jeffrey Holzgrafe et al. “Cavity electro-optics in thin-film lithium niobate for efficient microwave-to-optical transduction”. In: *Optica* 7.12 (Dec. 2020), pp. 1714–1720. DOI: 10.1364/OPTICA.397513. URL: http://www.osapublishing.org/optica/abstract.cfm?URI=optica-7-12-1714.

[3] Qing-Yuan Zhao et al. “Single-photon imager based on a superconducting nanowire delay line”. en. In: *Nature Photon* 11.4 (Apr. 2017). Number: 4 Publisher: Nature Publishing Group, pp. 247–251. ISSN: 1749-4893. DOI: 10.1038/nphoton.2017.35. URL: http://www.nature.com/articles/nphoton.2017.35 (visited on 02/25/2022).

[4] Jeffrey M. Shainline et al. “Superconducting Optoelectronic Circuits for Neuromorphic Computing”. In: *Phys. Rev. Applied* 7.3 (Mar. 2017). Publisher: American Physical Society, p. 034013. DOI: 10.1103/PhysRevApplied.7.034013. URL: https://link.aps.org/doi/10.1103/PhysRevApplied.7.034013 (visited on 03/16/2022).

[5] Martin G. Blaber, Matthew D. Arnold, and Michael J. Ford. “Search for the Ideal Plasmonic Nanoshell: The Effects of Surface Scattering and Alternatives to Gold and Silver”. en. In: *The Journal of Physical Chemistry C* 113.8 (Feb. 2009), pp. 3041–3045. ISSN: 1932-7447, 1932-7455. DOI: 10.1021/jp810808h. URL: https://pubs.acs.org/doi/10.1021/jp810808h (visited on 01/05/2022).

[6] Natsuki Mori. “Superconductivity in transparent Sn-doped In2O3 films”. In: *Journal of Applied Physics* 73.3 (Feb. 1993). Publisher: American Institute of Physics, pp. 1327–1338. ISSN: 0021-8979. DOI: 10.1063/1.353251. URL: https://aip.scitation.org/doi/10.1063/1.353251 (visited on 09/02/2021).

[7] Ali E. Aliev et al. “Reversible superconductivity in electrochromic indium-tin oxide films”. In: *Appl. Phys. Lett.* 101.25 (Dec. 2012). Publisher: American Institute of Physics, p. 252603. ISSN: 0003-6951. DOI: 10.1063/1.4772536. URL: https://aip.scitation.org/doi/10.1063/1.4772536 (visited on 06/01/2021).

[8] Alfredo Rueda et al. “Efficient microwave to optical photon conversion: an electro-optical realization”. EN. In: *Optica, OPTICA* 3.6 (June 2016). Publisher: Optica Publishing Group, pp. 597–604. ISSN: 2334-2536. DOI: 10.1364/OPTICA.3.000597. URL: https://opg.optica.org/optica/abstract.cfm?uri=optica-3-6-597 (visited on 02/25/2022).

[9] Nicholas J. Lambert et al. “Coherent Conversion Between Microwave and Optical Photons—An Overview of Physical Implementations”. en. In: *Advanced Quantum Technologies* 3.1 (2020), p. 1900077. ISSN: 2511-9044. DOI: 10.1002/qute.201900077. URL: https://onlinelibrary.wiley.com/doi/abs/10.1002/qute.201900077 (visited on 03/17/2022).

[10] R. Barends et al. “Minimizing quasiparticle generation from stray infrared light in superconducting quantum circuits”. In: *Appl. Phys. Lett.* 99.11 (Sept. 2011). Publisher: American Institute of Physics, p. 113507. ISSN: 0003-6951. DOI: 10.1063/1.3638063. URL: http://aip.scitation.org/doi/full/10.1063/1.3638063 (visited on 02/25/2022).

[11] J.B. DuBow, D.E. Burk, and J.R. Sites. “Solar cells of indium tin oxide on silicon”. In: *1975 International Electron Devices Meeting*. 1975, pp. 230–232. DOI: 10.1109/IEDM.1975.188867.

[12] Cheol Hwan Kim et al. “Fabrication of Structurally Simple Index-Matched ITO Films Using Roll-to-Roll Sputtering for Touch Screen Panel Devices”. en. In: *Plasma Processes and Polymers* 12.11 (2015), pp. 1322–1327. ISSN: 1612-8869. DOI: 10.1002/ppap.201500057. URL: http://onlinelibrary.wiley.com/doi/abs/10.1002/ppap.201500057 (visited on 12/20/2021).

[13] Millie Dresselhaus. *6.732 Solid State Physics II Notes*. URL: http://web.mit.edu/6.732/www/opt.pdf.

[14] Huanyu Zhou and Jin-Woo Park. "Effect of the crystallinity of indium tin oxide on the charge transfer at the interfaces and the performances of flexible organic light emitting diodes". en. In: *physica status solidi (a)* 212.2 (2015), pp. 414–424. ISSN: 1862-6319. DOI: 10.1002/pssa.201431550. URL: http://onlinelibrary.wiley.com/doi/abs/10.1002/pssa.201431550 (visited on 03/10/2022).

[15] Masayuki Kanehara et al. "Indium Tin Oxide Nanoparticles with Compositionally Tunable Surface Plasmon Resonance Frequencies in the Near-IR Region". In: *J. Am. Chem. Soc.* 131.49 (Dec. 2009). Publisher: American Chemical Society, pp. 17736–17737. ISSN: 0002-7863. DOI: 10.1021/ja9064415. URL: https://doi.org/10.1021/ja9064415 (visited on 03/15/2022).

[16] Eugene Hecht. *Optics*. eng. Book Title: Optics Edition: 5 ed. ISBN: 9780133977226 Place: Boston. 2017.

[17] P Bousquet. "Etude theorique des proprietes optiques des couches minces transparentes". In: *Annales de physique* 13 (1957), pp. 5–15.

[18] E. Bustarret. "Superconductivity in doped semiconductors". en. In: *Physica C: Superconductivity and its Applications*. Superconducting Materials: Conventional, Unconventional and Undetermined 514 (July 2015), pp. 36–45. ISSN: 0921-4534. DOI: 10.1016/j.physc.2015.02.021. URL: https://www.sciencedirect.com/science/article/pii/S0921453415000489 (visited on 03/09/2022).

[19] C. S. Koonce. "Theory of Superconducting Semiconductors". en. In: *The Science and Technology of Superconductivity*. Ed. by W. D. Gregory, W. N. Mathews, and E. A. Edelsack. Boston, MA: Springer US, 1973, pp. 373–387. ISBN: 978-1-4684-2997-8. DOI: 10.1007/978-1-4684-2997-812.

[20] N. F. (Nevill Francis) Mott. *Metal-insulator transitions*. eng. London: Taylor I& Francis, 1974. ISBN: 0850660793.

[21] Akira Ikushima and Takao Mizusaki. "Superconductivity in niobium and niobium-tantalum alloys". en. In: *Journal of Physics and Chemistry of Solids* 30.4 (Apr. 1969), pp. 873–879. ISSN: 0022-3697. DOI: 10.1016/0022-3697(69)90283-2. URL: https://www.

sciencedirect.com/science/article/pii/0022369769902832 (visited on 02/18/2022).

[22] J. K. Hulm et al. "Chapter 5 Superconductivity in Semiconductors and Semi-Metals". en. In: *Progress in Low Temperature Physics*. Ed. by C. J. Gorter. Vol. 6. Elsevier, Jan. 1970, pp. 205–242. DOI: 10.1016/S0079-6417(08)60064-5. URL: https://www.sciencedirect.com/science/article/pii/S0079641708600645 (visited on 02/18/2022).

[23] P. W. Anderson. "Theory of dirty superconductors". en. In: *Journal of Physics and Chemistry of Solids* 11.1 (Sept. 1959), pp. 26–30. ISSN: 0022-3697. DOI: 10.1016/0022-3697(59)90036-8. URL: https://www.sciencedirect.com/science/article/pii/0022369759900368 (visited on 02/22/2022).

[24] W. L. McMillan. "Transition Temperature of Strong-Coupled Superconductors". In: *Physical Review* 167.2 (Mar. 1968). Publisher: American Physical Society, pp. 331–344. DOI: 10.1103/PhysRev.167.331. URL: https://link.aps.org/doi/10.1103/PhysRev.167.331 (visited on 02/22/2022).

[25] J. K. Hulm et al. "Superconducting Interactions in Tin Telluride". In: *Physical Review* 169.2 (May 1968). Publisher: American Physical Society, pp. 388–394. DOI: 10.1103/PhysRev.169.388. URL: https://link.aps.org/doi/10.1103/PhysRev.169.388 (visited on 02/22/2022).

[26] Tanmoy Das and Kapildeb Dolui. "Superconducting dome in MoS 2 and TiSe 2 generated by quasiparticle-phonon coupling". en. In: *Phys. Rev. B* 91.9 (Mar. 2015), p. 094510. ISSN: 1098-0121, 1550-235X. DOI: 10.1103/PhysRevB.91.094510. URL: https://link.aps.org/doi/10.1103/PhysRevB.91.094510 (visited on 08/30/2021).

[27] Xiang-Long Yu and Jiansheng Wu. "Superconducting dome driven by intervalley phonon scattering in monolayer MoS_2". en. In: *New Journal of Physics* 22.1 (Jan. 2020), p. 013015. ISSN: 1367-2630. DOI: 10.1088/1367-2630/ab5cce. URL: https://iopscience.iop.org/article/10.1088/1367-2630/ab5cce (visited on 08/27/2021).

[28] K. Ueno et al. “Discovery of superconductivity in KTaO3 by electrostatic carrier doping”. en. In: *Nature Nanotechnology* 6.7 (July 2011). ISSN: 1748-3395. URL: https://www.nature.com/articles/nnano.2011.78 (visited on 08/27/2021).

[29] Marvin L. Cohen. “Superconductivity in Many-Valley Semiconductors and in Semimetals”. en. In: *Physical Review* 134.2A (Apr. 1964), A511–A521. ISSN: 0031-899X. DOI: 10.1103/PhysRev.134.A511. URL: https://link.aps.org/doi/10.1103/PhysRev.134.A511 (visited on 02/22/2022).

[30] C. S. Koonce et al. “Superconducting Transition Temperatures of Semiconducting SrTiO3”. In: *Physical Review* 163.2 (Nov. 1967). Publisher: American Physical Society, pp. 380–390. DOI: 10.1103/PhysRev.163.380. URL: https://link.aps.org/doi/10.1103/PhysRev.163.380 (visited on 02/22/2022).

[31] J. F. Schooley et al. “Dependence of the Superconducting Transition Temperature on Carrier Concentration in Semiconducting SrTi O 3”. en. In: *Physical Review Letters* 14.9 (Mar. 1965), pp. 305–307. ISSN: 0031-9007. DOI: 10.1103/PhysRevLett.14.305. URL: https://link.aps.org/doi/10.1103/PhysRevLett.14.305 (visited on 02/22/2022).

[32] Tyuzi Ohyama, Minoru Okamoto, and Eizo Otsuka. “Weak Localization and Correlation Effects in Indium-Tin-Oxide Films. II. Two-to-Three Dimensional Transition and Competition between Localization and Superconductivity”. In: *J. Phys. Soc. Jpn.* 54.3 (Mar. 1985). Publisher: The Physical Society of Japan, pp. 1041–1053. ISSN: 0031-9015. DOI: 10.1143/JPSJ.54.1041. URL: https://journals.jps.jp/doi/10.1143/JPSJ.54.1041 (visited on 02/23/2022).

[33] Tyuzi Ohyama, Minoru Okamoto, and Eizo Otsuka. “Weak Localization and Correlation Effects of Two Dimensional Electrons in Indium-Tin-Oxide Films”. In: *J. Phys. Soc. Jpn.* 52.10 (Oct. 1983). Publisher: The Physical Society of Japan, pp. 3571–3578. ISSN: 0031-9015. DOI: 10.1143/JPSJ.52.3571. URL: https://journals.jps.jp/doi/10.1143/JPSJ.52.3571 (visited on 02/23/2022).

[34] Shao-Pin Chiu et al. “Four-probe electrical-transport measurements on single indium tin oxide nanowires between 1.5 and 300 K”. en. In: *Nanotechnology* 20.10 (Mar. 2009), p. 105203.

ISSN: 0957-4484, 1361-6528. DOI: 10.1088/0957-4484/20/10/105203. URL: https://iopscience.iop.org/article/10.1088/0957-4484/20/10/105203 (visited on 08/26/2021).

[35] Ali E. Aliev, Monica Jung de Andrade, and Myron B. Salamon. "Paramagnetic Meissner Effect in Electrochemically Doped Indium-Tin Oxide Films". en. In: *J Supercond Nov Magn* 29.7 (July 2016), pp. 1793–1803. ISSN: 1557-1947. DOI: 10.1007/s10948-016-3501-7. URL: https://doi.org/10.1007/s10948-016-3501-7 (visited on 06/15/2021).

[36] A. E. Koshelev and A. I. Larkin. "Paramagnetic moment in field-cooled superconducting plates: Paramagnetic Meissner effect". en. In: *Phys. Rev. B* 52.18 (Nov. 1995), pp. 13559–13562. ISSN: 0163-1829, 1095-3795. DOI: 10.1103/PhysRevB.52.13559. URL: https://link.aps.org/doi/10.1103/PhysRevB.52.13559 (visited on 02/25/2022).

[37] David Kowal and Zvi Ovadyahu. "Disorder induced granularity in an amorphous superconductor". en. In: *Solid State Communications* 90.12 (June 1994), pp. 783–786. ISSN: 0038-1098. DOI: 10.1016/0038-1098(94)90242-9. URL: https://www.sciencedirect.com/science/article/pii/0038109894902429 (visited on 06/01/2021).

[38] Yonatan Dubi, Yigal Meir, and Yshai Avishai. "Nature of the superconductor–insulator transition in disordered superconductors". en. In: *Nature* 449.7164 (Oct. 2007), pp. 876–880. ISSN: 1476-4687. DOI: 10.1038/nature06180. URL: https://www.nature.com/articles/nature06180 (visited on 03/25/2022).

[39] Myles Steiner and Aharon Kapitulnik. "Superconductivity in the insulating phase above the field-tuned superconductor–insulator transition in disordered indium oxide films". en. In: *Physica C: Superconductivity* 422.1 (May 2005), pp. 16–26. ISSN: 0921-4534. DOI: 10.1016/j.physc.2005.02.014. URL: https://www.sciencedirect.com/science/article/pii/S0921453405000894 (visited on 06/01/2021).

[40] Sreemanta Mitra et al. "Negative Magnetoresistance in Amorphous Indium Oxide Wires". en. In: *Sci Rep* 6.1 (Nov. 2016), p. 37687. ISSN: 2045-2322. DOI: 10.1038/srep37687. URL: https://www.nature.com/articles/srep37687 (visited on 03/25/2022).

[41] Chin-Ying Chen, Jyh-Jier Ho, and Robert Y. Hsiao. "Performance evaluation of the indium zinc oxide (IZO) thin films for organic electroluminescent diode applications". In: *ACOFT/AOS 2006 - Australian Conference on Optical Fibre Technology/Australian Optical Society*. July 2006, pp. 36–38. DOI: 10.1109/ACOFT.2006.4519242.

[42] N. Ito et al. "Electrical and optical properties of amorphous indium zinc oxide films". en. In: *Thin Solid Films*. Proceedings of the Fourth International Symposium on Transparent Oxide Thin Films for Electronics and Optics (TOEO-4) 496.1 (Feb. 2006), pp. 99–103. ISSN: 0040-6090. DOI: 10.1016/j.tsf.2005.08.257. URL: https://www.sciencedirect.com/science/article/pii/S0040609005015063 (visited on 02/23/2022).

[43] Kazumasa Makise et al. "Superconductivity in transparent zinc-doped In $_2$ O $_3$ films having low carrier density". en. In: *Science and Technology of Advanced Materials* 9.4 (Dec. 2008), p. 044208. ISSN: 1468-6996, 1878-5514. DOI: 10.1088/1468-6996/9/4/044208. URL: http://www.tandfonline.com/doi/full/10.1088/1468-6996/9/4/044208 (visited on 08/16/2021).

[44] Takeo Ohsawa et al. "Origin of Optical Transparency in a Transparent Superconductor LiTi2O4". In: *ACS Appl. Electron. Mater. 2, 517-522* (2012).

[45] Hiroshi Kawazoe and Kazushige Ueda. "Transparent Conducting Oxides Based on the Spinel Structure". en. In: *Journal of the American Ceramic Society* 82.12 (1999), pp. 3330–3336. ISSN: 1551-2916. DOI: 10.1111/j.1151-2916.1999.tb02247.x. URL: https://onlinelibrary.wiley.com/doi/abs/10.1111/j.1151-2916.1999.tb02247.x (visited on 02/23/2022).

[46] D. C. Johnston et al. "High temperature superconductivity in the LiTiO ternary system". en. In: *Materials Research Bulletin* 8.7 (July 1973), pp. 777–784. ISSN: 0025-5408. DOI: 10.1016/0025-5408(73)90183-9. URL: https://www.sciencedirect.com/science/article/pii/0025540873901839 (visited on 02/23/2022).

[47] D. C. Johnston. "Superconducting and normal state properties of Li1+xTi2-xO4 spinel compounds. I. Preparation, crystallography, superconducting properties, electrical resistivity, dielectric behavior, and magnetic susceptibility". en. In: *J Low Temp Phys* 25.1 (Oct. 1976),

pp. 145–175. ISSN: 1573-7357. DOI: 10.1007/BF00654827. URL: https://doi.org/10.1007/BF00654827 (visited on 02/23/2022).

[48] Evagelia G. Moshopoulou. "Superconductivity in the Spinel Compound LiTi2O4". en. In: *Journal of the American Ceramic Society* 82.12 (Dec. 2004), pp. 3317–3320. ISSN: 00027820, 15512916. DOI: 10.1111/j.1151-2916.1999.tb02245.x. URL: https://onlinelibrary.wiley.com/doi/10.1111/j.1151-2916.1999.tb02245.x (visited on 11/24/2021).

[49] Takeo Ohsawa et al. "Origin of Optical Transparency in a Transparent Superconductor LiTi2O4". In: *ACS Applied Electronic Materials* 2.2 (Feb. 2020). Publisher: American Chemical Society, pp. 517–522. DOI: 10.1021/acsaelm.9b00751. URL: https://doi.org/10.1021/acsaelm.9b00751 (visited on 11/24/2021).

[50] Takuto Soma, Kohei Yoshimatsu, and Akira Ohtomo. "p-type transparent superconductivity in a layered oxide". In: *AAAS Science Advances* (2020).

[51] Tivadar Lohner et al. "Optical analysis of room temperature magnetron sputtered ITO films by reflectometry and spectroscopic ellipsometry". In: *Journal of Materials Research* (2014).

[52] Yeon Sik Jung. "Spectroscopic ellipsometry studies on the optical constants of indium tin oxide films deposited under various sputtering conditions". In: *Thin Solid Films* (2004).

[53] Masayuki Kamei et al. "Heteroepitaxial growth of tin-doped indium oxide films on single crystalline yttria stabilized zirconia substrates". en. In: *Applied Physics Letters* 64.20 (May 1994), pp. 2712–2714. ISSN: 0003-6951, 1077-3118. DOI: 10.1063/1.111474. URL: http://aip.scitation.org/doi/10.1063/1.111474 (visited on 02/22/2022).

[54] Naoaki Taga et al. "Electrical properties of heteroepitaxial grown tin-doped indium oxide films". en. In: *Journal of Applied Physics* 80.2 (July 1996), pp. 978–984. ISSN: 0021-8979, 1089-7550. DOI: 10.1063/1.362910. URL: http://aip.scitation.org/doi/10.1063/1.362910 (visited on 02/22/2022).

[55] Allen J. Bard. *Electrochemical methods : fundamentals and applications*. eng. 2nd ed. New York: John Wiley, 2001. ISBN: 0471043729.

[56] David B. Williams and C. Barry Carter. “The Transmission Electron Microscope”. en. In: *Transmission Electron Microscopy: A Textbook for Materials Science*. Ed. by David B. Williams and C. Barry Carter. Boston, MA: Springer US, 2009, pp. 3–22. ISBN: 978-0-387-76501-3. DOI: 10.1007/978-0-387-76501-31. URL: https://doi.org/10.1007/978-0-387-76501-31 (visited on 03/23/2022).

[57] Paul van der Heide. *X-Ray Photoelectron Spectroscopy*. John Wiley I& Sons, Ltd, 2011. ISBN: 9781118162897. DOI: https://doi.org/10.1002/9781118162897. URL: https://onlinelibrary.wiley.com/doi/abs/10.1002/9781118162897.

[58] Semilab. *SE-2000 Manual 2020*.

[59] Zheng Fan. “Hydrogen plasma exposure of In/ITO bilayers as an effective way for dispersing In nanoparticles”. In: *arXiv:1611.05606 [cond-mat]* (Mar. 2017). arXiv: 1611.05606. URL: http://arxiv.org/abs/1611.05606 (visited on 08/17/2021).

[60] R. X. Wang et al. “Influence of annealing temperature and environment on the properties of indium tin oxide thin films”. en. In: 38.12 (June 2005). Publisher: IOP Publishing, pp. 2000–2005. ISSN: 0022-3727. DOI: 10.1088/0022-3727/38/12/022. URL: https://doi.org/10.1088/0022-3727/38/12/022 (visited on 11/12/2021).

[61] Sarra Bouden et al. “Multifunctional Indium Tin Oxide Electrode Generated by Unusual Surface Modification”. en. In: *Sci Rep* 6.1 (Nov. 2016), p. 36708. ISSN: 2045-2322. DOI: 10.1038/srep36708. URL: https://www.nature.com/articles/srep36708 (visited on 08/26/2021).

[62] Liang Liu et al. “Important Implications of the Electrochemical Reduction of ITO”. en. In: *Electrochimica Acta* 176 (Sept. 2015), pp. 1374–1381. ISSN: 0013-4686. DOI: 10.1016/j.electacta.2015.07.129. URL: https://www.sciencedirect.com/science/article/pii/S0013468615301961 (visited on 08/23/2021).

[63] K. Oura et al. “Growth of Thin Films”. en. In: *Surface Science: An Introduction*. Ed. by K. Oura et al. Advanced Texts in Physics. Berlin, Heidelberg: Springer, 2003, pp. 357–387. ISBN: 978-3-662-05179-5. DOI: 10.1007/978-3-662-05179-514. URL: https://doi.org/10.1007/978-3-662-05179-514 (visited on 02/11/2022).

[64] Peter M. M. C. Bressers and Eric A. Meulenkamp. “The Electrochromic Behavior of Indium Tin Oxide in Propylene Carbonate Solutions”. en. In: *J. Electrochem. Soc.* 145.7 (July 1998), pp. 2225–2231. ISSN: 0013-4651, 1945-7111. DOI: 10.1149/1.1838624. URL: https://iopscience.iop.org/article/10.1149/1.1838624 (visited on 03/15/2022).

[65] G. Guenther et al. “Formation of metallic indium-tin phase from indium-tin-oxide nanoparticles under reducing conditions and its influence on the electrical properties”. In: *Journal of Applied Physics* 104.3 (Aug. 2008). Publisher: American Institute of Physics, p. 034501. ISSN: 0021-8979. DOI: 10.1063/1.2958323. URL: https://aip.scitation.org/doi/full/10.1063/1.2958323 (visited on 01/24/2022).

[66] G. Frank and H. Köstlin. “Electrical properties and defect model of tin-doped indium oxide layers”. en. In: *Appl. Phys. A* 27.4 (Apr. 1982), pp. 197–206. ISSN: 1432-0630. DOI: 10.1007/BF00619080. URL: https://doi.org/10.1007/BF00619080 (visited on 02/14/2022).

[67] G. E. Jellison and F. A. Modine. “Parameterization of the optical functions of amorphous materials in the interband region”. en. In: *Appl. Phys. Lett.* 69.3 (July 1996), pp. 371–373. ISSN: 0003-6951, 1077-3118. DOI: 10.1063/1.118064. URL: http://aip.scitation.org/doi/10.1063/1.118064 (visited on 03/17/2022).

[68] Yongqian Li. “Optical Properties of Plasmonic Materials”. en. In: *Plasmonic Optics Theory and Applications*. SPIE PRESS, 2017. ISBN: 978-1-5106-0757-6. DOI: 10.1117/3.2263757.ch1. URL: http://ebooks.spiedigitallibrary.org/content.aspx?bookid=2051&sectionid=153917732 (visited on 03/31/2022).

[69] H.-L. Zhang, S. D. Evans, and J. R. Henderson. “Spectroscopic Ellipsometric Evaluation of Gold Nanoparticle Thin Films Fabricated Using Layer-by-Layer Self-Assembly”. In: *Advanced Materials* 15.6 (2003), pp. 531–534. ISSN: 1521-4095. DOI: 10.1002/adma.200390124. URL: https://onlinelibrary.wiley.com/doi/abs/10.1002/adma.200390124 (visited on 08/24/2021).

[70] Miriam Carlberg et al. “Spectroscopic ellipsometry study of silver nanospheres and nanocubes in thin film layers”. en. In: *Opt. Mater. Express* 7.12 (Dec. 2017), p. 4241. ISSN: 2159-3930. DOI: 10.1364/OME.7.004241. (Visited on 08/24/2021).

[71] N. Biyikli et al. “ITO-Schottky photodiodes for high-performance detection in the UV-IR spectrum”. In: *IEEE Journal of Selected Topics in Quantum Electronics* 10.4 (July 2004). Conference Name: IEEE Journal of Selected Topics in Quantum Electronics, pp. 759–765. ISSN: 1558-4542. DOI: 10.1109/JSTQE.2004.833977.

[72] E Leksina, G P Motulevich, and A A Shubin. “THE OPTICAL PROPERTIES OF NIOBIUM”. en. In: (), p. 8.

[73] J. H. P. Watson. “Transition Temperature of Superconducting Indium, Thallium, and Lead Grains”. en. In: *Phys. Rev. B* 2.5 (Sept. 1970), pp. 1282–1286. ISSN: 0556-2805. DOI: 10.1103/PhysRevB.2.1282. URL: https://link.aps.org/doi/10.1103/PhysRevB.2.1282 (visited on 11/04/2021).

[74] W.-H. Li et al. “Enhancement of superconductivity by the small size effect in In nanoparticles”. en. In: *Phys. Rev. B* 72.21 (Dec. 2005), p. 214516. ISSN: 1098-0121, 1550-235X. DOI: 10.1103/PhysRevB.72.214516. URL: https://link.aps.org/doi/10.1103/PhysRevB.72.214516 (visited on 11/04/2021).

[75] Ying Zhang et al. “Dramatic enhancement of superconductivity in single-crystalline nanowire arrays of Sn”. en. In: *Sci Rep* 6.1 (Sept. 2016). ISSN: 2045-2322. DOI: 10.1038/srep32963. URL: https://www.nature.com/articles/srep32963 (visited on 11/04/2021).

[76] D. Kowal and Z. Ovadyahu. “Scale dependent superconductor–insulator transition”. en. In: *Physica C: Superconductivity*. Proceedings of the Workshop on Fluctuations and Phase Transitions in Superconductors 468.4 (Feb. 2008), pp. 322–325. ISSN: 0921-4534. DOI: 10.1016/j.physc.2007.07.012. URL: https://www.sciencedirect.com/science/article/pii/S0921453407013627 (visited on 06/01/2021).